

Multi-chromatic analysis polarimetric interferometric synthetic aperture radar (MCA-PollInSAR) for urban classification

Filippo Biondi

To cite this article: Filippo Biondi (2018): Multi-chromatic analysis polarimetric interferometric synthetic aperture radar (MCA-PollInSAR) for urban classification, International Journal of Remote Sensing

To link to this article: <https://doi.org/10.1080/01431161.2018.1552814>



Published online: 11 Dec 2018.



Submit your article to this journal



CrossMark

View Crossmark data



Multi-chromatic analysis polarimetric interferometric synthetic aperture radar (MCA-PollnSAR) for urban classification

Filippo Biondi

Department of Engineering, University of L'Aquila, L'Aquila, Italy

ABSTRACT

One of the problems of Synthetic Aperture Radar (SAR) polarimetric decomposition, is that oriented urban areas and vegetation signatures are decomposed into the same volume scattering mechanism. Such indetermination makes it difficult to distinguish vegetation from the oblique urban areas with respect to the radar illumination direction within the volume scattering mechanism. This event occurs because oriented targets exhibit similar polarimetric responses. This paper presents an improvement of the PolSAR decomposition scheme which permits the performing of more accurate classification. The method uses the information existing form the interference generated between two Doppler sub-aperture SAR images. This interferometric polarimetric SAR (PollnSAR) multi-chromatic analysis (MCA-PollnSAR) signal processing method permits the efficient separation of oriented buildings from vegetation yielding considerably improved results in which oriented urban areas are recognized, from volume scattering, as double-bounce objects. Results also show a considerable improvement in the robustness of classification and also in terms of definition and precision.

ARTICLE HISTORY

Received 5 March 2018
Accepted 17 September 2018

1. Introduction

Polarimetric synthetic aperture radar (SAR) (PolSAR) improves the target reconnaissance capabilities of SAR systems. A fully polarimetric radar sensor uses the scattered electric field vector orientation variation like a resource with respect to the transmitted information. These features are useful to extrapolate information about the electrical and mechanical proprieties of targets. Classification of the scattering mechanisms is one of the main fields of radar polarimetry. The problem of volume oriented mis-classification is solved using the polarimetric SAR interferometry (PollnSAR) method.

This type of SAR observation employs a couple of interferometric SAR images in order to produce a sufficient level of information useful to delete the volume-oriented indetermination. The problem is that the use of one interferometric SAR couple consists of employing two radars spatially separated by a small baseline (technological

redundancy implementation) or using one radar implementing a temporal repeat-pass strategy. Both solutions are expensive in terms of resources. This paper is proposing the multi-chromatic-analysis polarimetric interferometric SAR (MCA-PollnSAR) signal processing technique in order to avoid the acquisition of the interferometric observation and using only one Doppler large-band SAR image. This method will give massively advantage to the polarimetric remote sensing community in obtaining a very precise classification of SAR images and solving the volume-oriented mis-classification of urban areas. This task is done spending only one SAR image. Since writing this paper, very interesting research studies have been produced in the fields of polarimetric classification.

1.1. Polarimetric SAR classification

In Jong-Sen et al. (1999) an important study, regarding the unsupervised terrain classification, has been performed. The implemented technique used different polarimetric scattering mechanisms characteristics to preserve the purity of the dominant polarimetric scattering properties. In Jong-Sen et al. (2004) an unsupervised terrain classification algorithm using PolSAR imaged has been provided. The authors processed a combination of scattering models based for isolating the purity of dominant scattering proprieties. Results were estimated using the Jet Propulsion Laboratory's airborne synthetic aperture radar imaging instrument (AIRSAR) and the German Aerospace Center's E-SAR L-band PolSAR images. From the information given, the oriented volume indetermination still existed in a single full-polarimetric SAR image. This ambiguity was still present also when some ad-hoc polarimetric de-orientation models have been implemented. Polarization aspects of the radar target scattering problem have been successfully reexamined by Kostinski Alexander and Wolfgang-Martin (1986). The paper formulated a valid solution for the radar polarimetry optimization problem without the necessity of some target scattering operators for diagonalization and changing of basis. An efficient solution to solve the volume-oriented ambiguity was proposed by Chen et al. (2013) where the repeat-pass PollnSAR used coherence estimation to solve the oriented volume indetermination problem. PollnSAR coherence is sensitive if considering some different types of forests and terrains. Research performed by Chen et al. (2014) and Chen et al. (2013) showed a double- and odd-bounce scattering models which have been generalized to fit the cross-polarization and off-diagonal terms, by separating their independent orientation angles. Authors proposed a general decomposition framework that used all the coherency matrix elements. The residual minimization criterion was used for the model inversion. In Tao et al. (2017) a feature selection scheme was established and a set of hidden polarimetric features has been selected in the rotation domain. A classification method was developed using the complementary information between roll-invariant and selected hidden polarimetric features with a support vector machine and using an efficient decision tree classifier.

1.2. Multi-component polarimetric SAR decomposition

In Robert and Pottier (1997) an important work regarding an entropy based classification scheme for the land application of PolSAR has been performed. The using of statistical methods relies on a coherency matrix eigenvalue analysis, successfully employing the

Bernoulli statistical model to estimate the average target scattering matrix parameter. In Van Zyl (1993) Cloude's PolSAR decomposition method has been successfully applied to vegetated data. In Ridha (2007) a target scattering model in terms of roll-invariant target parameters has been developed. Results were estimated processing the Convair-580 SAR images collected over the Ramsar Mer Bleue wetland site of Ottawa (Canada). In Anthony and Durden Stephen (1998) a three-component scattering model for PolSAR data has been developed. The first mechanism was the canopy modelled like a distributed target constituted by a cloud of randomly oriented dipoles. The second was the double-bounce scatter which was modelled by two orthogonal surfaces having different dielectric constants and the last one was the Bragg scattering from a moderately rough surface. In Yamaguchi et al. (2005) a four-component scattering model was proposed to decompose PolSAR images. The scheme extended the three-component decomposition strategy introduced in Freeman (2007) where the helix scattering power was added in the model to be the fourth polarimetric scattering event component. The work performed by Yamaguchi et al. (2006) was an extension of the Freeman, (1998) and the An et al. (2010) works where the four-component decomposition scheme has been estimated studying the polarimetric coherency matrix. The same decomposition results showed in Yamaguchi et al. (2005) has been obtained. In Freeman (2007) a two-component scattering mechanism model was fitted into the PolSAR investigation method used to observe forests. The first model was the canopy scatter with azimuthal symmetry and the double-bounce or the Bragg scattering from a moderately rough surface. In An et al. (2010) an improved three-component decomposition was proposed. The main innovation was the designation of a de-orientation process applied to the coherency matrix before it was decomposed into three scattering components. In Van Zyl et al. (2011) a model-based decomposition of polarimetric radar covariance matrices has been developed. The authors proposed a simple modification ensuring that all the covariance matrices in the decomposition should not have non-negative eigenvalues in order to better distinguish the basis polarimetric scattering mechanism. In Elise, Ccile, and Tabbara (2006) a de-orientation theory of polarimetric scattering targets was presented. The model was designed using a transformation of the target scattering vector, the target orientation was turned to a certain fixed state and polarimetric scattering of the transformed scattering vector. Results showed the prominence of a generic characteristic of the target. In Chen et al. (2013), a de-orientation effect investigation of oriented urban areas was presented. The work stated that de-orientation processing has been incorporated into the model-based decomposition to threat the overestimation of volume scattering contribution, by performing the coherency matrix rotation finalized to minimize the cross-polarization terms. In Lee, Schuler, and Ainsworth (2000) the problem of PolSAR data correction for changes in radar cross sections, which are caused by azimuth slopes has been addressed. The purpose of the work was to improve the accuracy of the geophysical parameter estimation techniques. SAR polarimetry could also be used to measure topography considering the polarimetric orientation angle. Lee et al. (2002) performed a work aimed to support some topographic measurements and the accurate estimation of geophysical parameters on rugged terrain areas using multi-baseline fully polarimetric SAR data. In order to support these applications, was found very important to accurately estimate the shifts in orientation angles induced by the azimuthal slope variations. The polarization orientation angle

of the scattering media affected the polarimetric radar signatures. In Lee et al. (2011) the effects of the orientation angle compensation on the coherency matrix and the polarimetric target decomposition have been studied. In Yamaguchi et al. (2011) authors presented an improvement of a decomposition scheme for the accurate classification of PolSAR images using the rotation of the coherency matrix which was useful to minimize the cross-polarized component. The work was performed to distinguish the vegetation from the oblique urban areas with respect to the radar direction of illumination within the volume scattering mechanism. The technique improved accurate results that oriented urban areas are recognized as double bounce objects from the volume scattering. In Singh et al. (2013) a new general four-component scattering power decomposition method, by implementing a set of unitary transformation for the polarimetric coherency matrix, has been proposed. It was found that this process enhanced the double-bounce scattering contribution over the urban areas compared to the existing methods. In Cloude et al. (1998) the SAR interferometry technique has been mixed with PolSAR. The author proposed a general formulation of the vector wave interferometry, including the conventional scalar interferometry like a special case. The work showed also a polarimetric basis transformation that could be introduced into SAR interferometry. The author proposed also how the polarimetric basis transformations were introduced into SAR interferometry and applied in order to form interferograms between all possible linear combinations of polarization states. The author formulated a simplified stochastic scattering model tested on dense forests demonstrating the effectiveness of the proposed algorithms. In this way, it was also demonstrated the importance of wave polarization for the physical interpretation of SAR interferograms. In Ballester et al. (2010) the Freeman-Durden the polarimetric decomposition concept theorized in Freeman et al. (2005) was adapted to PollnSAR data. The covariance matrix obtained from the PollnSAR observations was decomposed into three scattering mechanism matrices which were proposed in Freeman (2007). The objective was to describe each interferometric cross-correlation as the sum of the contributions corresponding to single-bounce, double-bounce, and random volume scattering processes. The PollnSAR coherence (Chen et al. 2013), which contains the full set of polarimetric and interferometric information, is an important source for a number of applications. The PollnSAR coherence is strongly polarimetric dependent and the general coherence optimization has been thoroughly investigated for the single and the multi-baseline PollnSAR configurations (Singh et al. 2013), (Neumann et al. 2008) and (Colin et al. 2006). Based on PollnSAR complex coherence together with some physical models, the surface and the volume scattering centres in the vertical direction can be separated, and biophysical parameters such as vegetation height are well reconstructed (Papathanassiou et al. 2001)-(Neumann et al. 2010). Additionally, polarization coherence tomography, which employs the variation of the interferometric coherence with the polarization and used to reconstruct cross-slab-range profiles functions in penetrable volume extended targets (Cloude 2006) and (Cloude 2007). Simultaneously, PollnSAR coherence was a good descriptor associated with the physical properties of different targets as cited in Singh et al. (2013). Environments containing forests can probably suffer from the temporal decorrelation which induces the showing of lower coherence in magnitude. The using of polarimetry permits to built-up areas containing more permanent scatterers (Ferretti et al. 2001a). In addition, a recent research work verified that the PollnSAR coherence

exhibits a close relationship between different forest structures (Ferro-Famil et al. 2001a) and (Ferro-Famil et al. 2005) which can be further explored for more accurate parameters retrieval (Laurent and Maxim 2008) and (Lee et al. 1999).

1.3. Polarimetric classification and convolutional neural networks

Research performed by Chen and Tao (2018) advanced deep learning techniques represented by a deep convolutional neural network (CNN) has been used to enhance the classification performance. The work attempt to contribute in incorporating expert knowledge of target scattering mechanism interpretation and polarimetric feature mining to assist deep CNN classifier training and improving the final classification performance. Both classical roll-invariant polarimetric features and hidden polarimetric features in the rotation domain have been used to drive an alternative deep CNN model. For multi-temporal unmanned aerial vehicle synthetic aperture radar (UAVSAR) data sets, the proposed scheme achieves comparably high classification accuracy as the normal CNN process for train-used temporal data, while for train-not-used data it obtains higher overall accuracy than the normal CNN method.

1.4. Synthetic aperture radar frequency diversity

The use of MCA generates sufficiently independent information which is based on the Doppler sub-apertures SAR refocusing. Such diversity is sufficient to estimate infra-chromatic complex coherencies which are processed to delete the volume-oriented scattering indetermination. The computational core of this technique starts from focusing only on one PolSAR image. The data are composed of one set of PolSAR images in the HH, HV, VH and VV polarizations, in the single look complex (SLC) format which are generated by focusing the native SAR images by correlation of two adaptive filters (the filter is dimensioned for the fast-time and the second is used to focus the slow-time after range migration). Usually, it is difficult for companies and space agencies delivering to principal investigators raw data. The author tested the proposed MCA strategy only using the SLC SAR data. A pseudo-raw has been estimated for each polarization and successfully the MCA approach was applied. This solution is found to be better than the solution proposed in Ferro-Famil et al. (2001b) because it needs only one SAR product, rather than two multi-temporal SAR images, observed between a spatial baseline. This new approach uses two fully polarimetric products, refocused using only one native full-pol raw wide-band observation. The MCA refocusing strategy produces a small azimuthal resolution loss, proportional to the loss of the Doppler portion band, not included in the slow-time matched filter. The SAR sub-products refocused according to the spectral scheme, are depicted in Figure 1. In Bovenga et al. (2013) the authors tested the MCA using some InSAR images and processing several range sub-apertures. This procedure permitted the exploiting of phase trend in each pixel as a function of the different central carrier frequencies to estimate the absolute optical path difference. The approach allows retrieving unambiguous height information on selected pixels, potentially solving the problem of spatial phase unwrapping, which is instead critical in the standard monochromatic approach. Experimental results confirmed the indications derived by the theoretical analysis, demonstrating the feasibility of the MCA absolute phase measurement, provided if a sufficient bandwidth is available. In (Duque et al. 2015) the authors presented a long single staring-

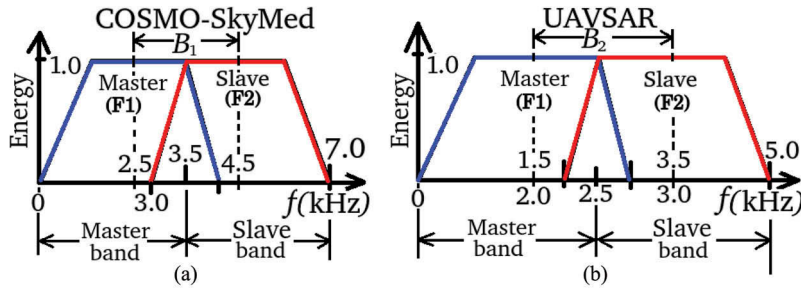


Figure 1. Frequency allocation planes. (a): COSMO-SkyMed study case. (b): UAVSAR study case.

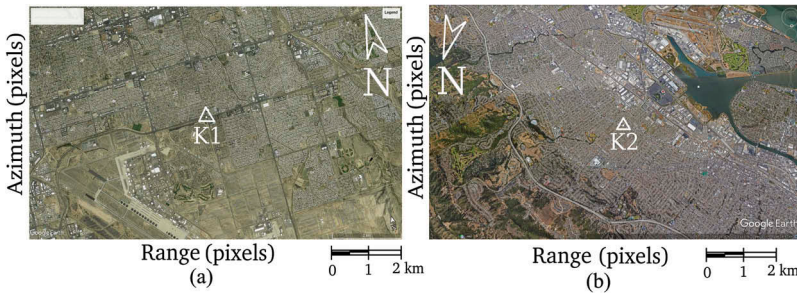


Figure 2. Optic images. (a): COSMO-SkyMed study case. (b): UAVSAR study case.

spotlight SAR TerraSAR-X acquisition which is a sufficient statistic to derive absolute heights on very highly coherent pixels. Two different results were presented in order to demonstrate that absolute heights can be retrieved using only one staring-spotlight SAR acquisition. The physical principle is measuring SAR defocusing effects due to long orbital curvatures. In Cloude et al. (1996) an interesting review of some polarimetric target decomposition was performed. Three main types of theorems were reviewed: those based on the Muller matrix and Stokes vector, those using the eigenvector analysis of the covariance and coherence matrices and those employing coherent decomposition of the scattering matrix. In Ferro-Famil et al. (2008) an unsupervised classification method of terrain types and man-made objects using PolSAR data has been provided. In order to initially classify the PolSAR image, the Cloude and Pottier's process to initially classify the PolSAR image has been used. In Ferro-Famil et al. (2001b) a new dual frequencies PolSAR classification scheme have been provided. The technique takes into account the processing of a (6×6) polarimetric coherency matrix handling the information from two images. These are applied to full polarimetric P, L, and C-bands SAR images providing high-performance results. In Chen et al. (2016) In Chen et al. (2016), a remote sensing full-PolSAR data set is used in order to give a quick response to large-scale natural disasters such as earthquakes and tsunami.

2. Methodology

Recent investigation has shown that imposing diversity on the radiation carrier frequency and on the Doppler history may give a new communication channel for more detailed information investigation (Bovenga et al. 2013) and (Moreira 1992). MCA was

developed for the first time in Madsen and Zebker (1992) and optimized in Bovenga et al. (2013) splitting the electromagnetic chirp band over multiple sub-apertures for absolute heights retrieval of interferometric SAR products which are ambiguous modulo 2π . MCA is also applied in the Doppler domain (Zhang et al. 2017) wherein most cases were used for conventional motion-compensation (MOCO) moving target indication (MTI) applications and for maritime surveillance (Biondi 2016).

2.1. Polarimetric coherency matrix estimation

According to Chen et al. (2012) and Chen et al. (2013), the coherence and covariance matrices of a polSAR image are given by:

$$\mathbf{T}_3 = \langle \mathbf{K} \cdot \mathbf{K}^\dagger \rangle \text{ and } \mathbf{C}_3 = \langle \boldsymbol{\Omega} \cdot \boldsymbol{\Omega}^\dagger \rangle. \quad (1)$$

where

$$\mathbf{T}_3 = \left\langle \begin{bmatrix} |\mathbf{K}_1|^2 & \mathbf{K}_1 \mathbf{K}_2^\dagger & \mathbf{K}_1 \mathbf{K}_3^\dagger \\ \mathbf{K}_2 \mathbf{K}_1^\dagger & |\mathbf{K}_2|^2 & \mathbf{K}_2 \mathbf{K}_3^\dagger \\ \mathbf{K}_3 \mathbf{K}_1^\dagger & \mathbf{K}_3 \mathbf{K}_2^\dagger & |\mathbf{K}_3|^2 \end{bmatrix} \right\rangle \text{ where}$$

$$|\mathbf{K}_1|^2 = \langle |\mathbf{S}_{HH} + \mathbf{S}_{VV}|^2 \rangle, |\mathbf{K}_2|^2 = \langle |\mathbf{S}_{HH} - \mathbf{S}_{VV}|^2 \rangle$$

$$\mathbf{K}_1 \mathbf{K}_2^\dagger = \langle (\mathbf{S}_{HH} + \mathbf{S}_{VV})(\mathbf{S}_{HH} - \mathbf{S}_{VV})^\dagger \rangle$$

$$\mathbf{K}_1 \mathbf{K}_3^\dagger = \langle (\mathbf{S}_{HH} + \mathbf{S}_{VV})2(\mathbf{S}_{HV})^\dagger \rangle$$

$$\mathbf{K}_2 \mathbf{K}_3^\dagger = \langle (\mathbf{S}_{HH} - \mathbf{S}_{HV})2(\mathbf{S}_{VV})^\dagger \rangle$$

$$\mathbf{K}_2 \mathbf{K}_1^\dagger = \langle (\mathbf{S}_{HH} - \mathbf{S}_{VV})(\mathbf{S}_{HH} + \mathbf{S}_{VV})^\dagger \rangle$$

$$\mathbf{K}_3 \mathbf{K}_1^\dagger = \langle 2(\mathbf{S}_{VV})(\mathbf{S}_{HH} + \mathbf{S}_{VV})^\dagger \rangle$$

$$\mathbf{K}_3 \mathbf{K}_2^\dagger = \langle 2(\mathbf{S}_{VV})(\mathbf{S}_{HH} - \mathbf{S}_{VV})^\dagger \rangle, |\mathbf{K}_3|^2 = \langle 4|\mathbf{S}_{HV}|^2 \rangle$$

and

$$\mathbf{K}_3 = [(\mathbf{S}_{HH} + \mathbf{S}_{VV})(\mathbf{S}_{HH} - \mathbf{S}_{VV})\sqrt{2}\mathbf{S}_{HV}]^\dagger$$

$$\mathbf{C}_3 = \langle \boldsymbol{\Omega} \cdot \boldsymbol{\Omega}^\dagger \rangle. \quad (2)$$

where

$$\mathbf{C}_3 = \left\langle \begin{bmatrix} |\boldsymbol{\Omega}_1|^2 & \boldsymbol{\Omega}_1 \boldsymbol{\Omega}_2^\dagger & \boldsymbol{\Omega}_1 \boldsymbol{\Omega}_3^\dagger \\ \boldsymbol{\Omega}_2 \boldsymbol{\Omega}_1^\dagger & |\boldsymbol{\Omega}_2|^2 & \boldsymbol{\Omega}_2 \boldsymbol{\Omega}_3^\dagger \\ \boldsymbol{\Omega}_3 \boldsymbol{\Omega}_1^\dagger & \boldsymbol{\Omega}_3 \boldsymbol{\Omega}_2^\dagger & |\boldsymbol{\Omega}_3|^2 \end{bmatrix} \right\rangle \text{ where} \quad (3)$$

$$|\Omega_1|^2 = \langle |\mathbf{S}_{\text{HH}}|^2 \rangle, |\Omega_2|^2 = 2\langle |\mathbf{S}_{\text{HV}}|^2 \rangle$$

$$|\Omega_3|^2 = \langle |\mathbf{S}_{\text{VV}}|^2 \rangle, \Omega_1 \Omega_2^\dagger = \sqrt{2} \langle \mathbf{S}_{\text{HH}} \mathbf{S}_{\text{HV}}^\dagger \rangle$$

$$\Omega_1 \Omega_3^\dagger = \langle \mathbf{S}_{\text{HH}} \mathbf{S}_{\text{VV}}^\dagger \rangle, \Omega_2 \Omega_1^\dagger = \sqrt{2} \langle \mathbf{S}_{\text{HV}} \mathbf{S}_{\text{HH}}^\dagger \rangle$$

$$\Omega_2 \Omega_3^\dagger = \sqrt{2} \langle \mathbf{S}_{\text{HV}} \mathbf{S}_{\text{VV}}^\dagger \rangle, \Omega_3 \Omega_1^\dagger = \langle \mathbf{S}_{\text{VV}} \mathbf{S}_{\text{HH}}^\dagger \rangle$$

$$\Omega_3 \Omega_2^\dagger = \sqrt{2} \langle \mathbf{S}_{\text{VV}} \mathbf{S}_{\text{HV}}^\dagger \rangle \text{ and}$$

$$\Omega = [\mathbf{S}_{\text{HH}} \sqrt{2} \mathbf{S}_{\text{HV}} \mathbf{S}_{\text{VV}}]^\dagger$$

In (2) the symbol $\langle \cdot \rangle$ is a spatial average operator. The parameter Ω is the polarimetric scattering vector in the (H = horizontal, V = vertical) polarimetric basis. The scattering vector is composed by the backscattering energy $\mathbf{S}_{\text{HH}, \text{HV and VV}}$ where the monostatic case assumption $\mathbf{S}_{\text{HV}=\text{VH}}$ has been imposed. The mathematical symbol \dagger is the Hermitian operator. The total scattering power of the polarimetric radar is:

$$\text{span} = \mathbf{S}_{11} + \mathbf{S}_{22} + \mathbf{S}_{33}. \quad (4)$$

The covariance matrix (4) permits the building of various models in order to decompose scattering events in scattering components (Lee et al. 1999), (Chen et al. 2013), (Robert and Pottier 1996), (Van Zyl 1993) and (Ridha 2007). The MCA analysis of SAR images permits the estimation of frequency diversity information. In the case of this paper, the author has used the MCA analysis signal processing similar to that described in Bovenga et al. (2013) but performed in the azimuth direction. The technique permits azimuth refocusing at different Doppler sub-bands, accepting a cross-range resolution loss. The azimuth resolution loss could be quantified approximately as 35% with respect to the total Doppler band amount. The author defines this new signal processing (SP) Approach as MCA-PollnSAR. The basic principle of MCA-PollnSAR is the diversification of view angles assumed from the radar anchored on a flying platform during a single SAR acquisition (Duque et al. 2015). SAR acquisitions can be performed from satellite platforms and airborne platforms. In this paper, the validation of the technique will be defined by processing two types of SAR data-sets. The first constitutes a multi-temporal fully-polarimetric satellite SAR dataset and the second is constituted by one airborne case fully-polarimetric data-set observed by the UAVSAR. The method proposed in this paper only requires a single SAR acquisition in order to delete the volume-oriented indetermination that appears when processing a single full polarimetric dataset. The MCA-PollnSAR approach bases its own functionality and consistency to flight trajectory and orbit inaccuracy in the airborne case. The principal reason which permits the azimuth high-resolution image formation is given by processing the Doppler frequency generated by the targets with respect to the platform motion. The higher the platform velocity is the wider the azimuth Doppler-rate band B_{az} will be. The generated Doppler-rate has the following configuration:

$$f_d = \frac{2v}{\lambda R_0}. \quad (5)$$

In (5) the parameter λ is the Radio-Frequency (RF) wavelength, the parameter \mathbf{R}_0 is the zero-Doppler range length. During the entire SAR acquisition, the zero-Doppler parameter variation is appreciated by the receiver, spanning un-layered contiguous range records constituting the raw data. This micro-Doppler capturing is the principal motivation for implementing the MCA-PollInSAR investigation approach treated in this paper. The layover indetermination appears after the focusing SP computational stage producing the SLC static image. Different chromatic products focused at different azimuth sub-bands and central bands can reveal hidden information due to the very small baselines produced by platform trajectory distortions and Doppler baselines due to sub-apertures analysis. Such distortions are present because in the atmosphere or in space, sensor platforms can never move on an ideal straight route. If second-order Taylor's parameters are introduced in the computational focusing machine, it is possible to estimate a complete range history \mathbf{R} . The first derivative of the parameter is the velocity $v = \mathbf{R}^{(1)}$ and its second derivative is the acceleration $v = \mathbf{R}^{(2)}$. When a chirped signal is transmitted from the sensor, an entire raw data back-scattering history, from each range-azimuth resolution cell, is stored in the memory. If the pattern error is sufficiently high, a height sensitivity is present due to the non-zero terms $v = \mathbf{R}^{(1)}$ and $v = \mathbf{R}^{(2)}$ that determine a non-ideal rectilinear motion of the sensor platform. Flight pattern errors in the airborne case are due to atmospheric resistance over the body of the plane. In the satellite case, the trajectory is not perfectly circular and parallel to the Earth and a kind of orbital distortion is so always present. Such effects are due to earth gravity field non-uniformity which name is usually J22-effect. In both cases, this error is a precise resource that generates a small Doppler-rate mismatch during the azimuth compression. Scatterers present in the same Cross Slant Range (CSR) ambiguous resolution-cell presents different Doppler rates due to the existence of a CSR platform motion component, velocity, and acceleration. However, the impulse response in the output of the azimuth matched filter is (Duque et al. 2015):

$$S(\omega_{az}) = \text{rect}\left(\frac{\omega_{az}(v)}{B_{az}}\right) \exp(-j\omega_{az}(v)t) \exp(-j\omega_{az_{CSR}}(v)t). \quad (6)$$

In (6) the parameter S is the impulse response at the output of the matched filter in the azimuth frequency domain, the symbol j is the imaginary unity number, the parameter ω_{az} is the azimuth frequency, the parameter B_{az} is the total azimuth bandwidth and the parameter t is the zero-Doppler azimuth time. Azimuth defocusing is introduced in the last exponential product weighted by the parameter $\omega_{az_{CSR}}$ which is proportional to the total Doppler Frequency Modulation rate, the FM rate mismatch and the total Doppler bandwidth. This MCA-PollInSAR approach aims to appreciate some spatial diversity from SAR defocusing due to the azimuth position variation of targets within different azimuth sub-apertures. Long azimuthal SAR apertures can be characterized to have high Linearly Frequency Modulation (LFM) rates. The displacement due to LRM mismatch, occurring at each target, in the k^{th} sub-aperture, existing in a certain range-azimuth resolution cell is equal to:

$$\Delta h_k = \frac{\delta \text{LFM}_{\text{rate}_k}}{\text{LFM}_{\text{rate}_k}^2} v_{\text{platform}} v_{\text{footprint}} \quad (7)$$

In (7) the parameter Δh_k is the centimetric displacement of a target in the k^{th} Doppler sub-aperture, the parameters $\delta \text{LFM}_{\text{rate}_k}$ and $\text{LFM}_{\text{rate}_k}$ are the FM rate mismatch and the total FM rate in the k^{th} azimuth sub-aperture. The parameters v_{platform} and $v_{\text{footprint}}$ are respectively the platform and the ground electromagnetic footprint velocities. The validation of the algorithm is confirmed by a successful estimation of infra-chromatic coherency data-sets directly dependent on the nature of the observed medium and the LFM mismatch observation. The azimuth frequency variation sampling is dependent on the survived Doppler band and the portion of the Doppler sub-aperture band loss. The basic principle of spectral diversity is the same as that considered to perform the PollInSAR principle used for robust polarimetric classification. The work treated in this paper is similar to the works performed in Chen et al. (2013); Colin et al. (2006); Lee et al. (1999) and Ferro-Famil et al. (2006) except for the PollInSAR case. The innovation proposed in this paper is that the interferometric data couple is produced using only one image, rather than using two images where the baselines are artificially designed using two repeat-pass observations. The Author constructed an MCA-PollInSAR Single Look Complex data couple, observed along one Doppler azimuth baseline, which was produced using the natural motion of the platform. This view angle variation produces a Doppler frequency proportional to the CSR velocity component, generating sufficient information useful for performing the MCA-PollInSAR unsupervised robust classification and mapping. The principal objective of the method is to delete the volume oriented mis-classification of urban areas and to perform precise classification and mapping. The processing scheme is organized to the following computational stages:

- (1) Couple of MCA-PollInSAR products estimation;
- (2) PolSAR classification of the full-band SLC product;
- (3) Series of optimized infra-chromatic coherencies estimation;
- (4) 6×6 MCA-PollInSAR matrix estimation;
- (5) Advanced robust polarimetric discrimination and segmentation.

The advanced classification treated in this paper, bases its functionality on the estimation of optimized infra-chromatic coherence maps. The Author demonstrates that this new information is useful to perform robust polarimetric discrimination of different scattering mechanisms that are impossible to resolve using only one single full-polarimetric SAR product. The efficiency of this new method is demonstrated using airborne and satellite data-sets. The different scattering mechanisms are segmented using a model-based, unsupervised classification algorithm. Figure 1(a,b) represents the frequency allocation plane constituted by refocusing the raw SAR image using two different sub-apertures. Both subproducts have less resolution respect to the original unique full-band product. In order to perform all the experiments, the author has produced two sub-products reducing of the 35% the total Doppler Band. the two refocused sub-bands are overlapped, according to the scheme depicted in Figure 3(a,b).

3. Multi-chromatic-analysis polarimetric SAR interferometry (MCA-PollInSAR)

In this paper explains an approach for designing an efficient unsupervised classification of Full-polarimetric SAR images. The technique uses the complementary polarimetric and multi-chromatic information of Laurent and Maxim (2008) and Duque et al. (2015). The results are

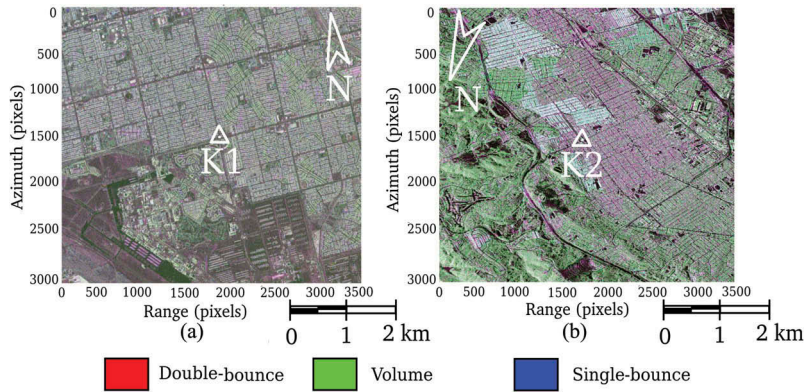


Figure 3. Full polarimetric SAR images. The red channel is generated by the HH-VV double-bounce. The blue channel is populated by the HH+VV single-bounce. The green channel is the volume HV + VH. (a): COSMO-SkyMed study case. (b): UAVSAR study case.

focused to perform an efficient volume de-orientation generated by oriented buildings respect to the radar Line of Sight. The classification is based on an optimized MCA interferometric coherence estimation useful to perform discrimination of different natural media that could not be achieved with the full-band focused polarimetric data. SAR systems are characterized by a dual frequency modulation (FM) while the FM parameters of transmitted pulse given by the range chirp are well known, the Doppler parameters (Doppler centroid and Doppler rate) are responsible to defocusing SAR image because of platform altitude variation and local atmosphere parameters variation. In Papathanassiou et al. (2001) the PollnSAR technique is developed. In that case, the interferometric condition is procured by a spatial baseline. MCA-PollnSAR use the frequency baseline concept where the multi-chromatic condition is performed in the Doppler domain. MCA-PollnSAR data, respect to conventional PollnSAR data, are formulated into a 6×6 dual-Doppler infra-chromatic interferometric coherency matrix. The MCA Sinclair matrices of two Doppler frequencies S_{f_1} and S_{f_2} are:

$$\mathbf{S}_{f_1} = \begin{bmatrix} \mathbf{S}_{HH_{f_1}} & \mathbf{S}_{HV_{f_1}} \\ \mathbf{S}_{VH_{f_1}} & \mathbf{S}_{VV_{f_1}} \end{bmatrix} \quad (8)$$

and

$$\mathbf{S}_{f_2} = \begin{bmatrix} \mathbf{S}_{HH_{f_2}} & \mathbf{S}_{HV_{f_2}} \\ \mathbf{S}_{VH_{f_2}} & \mathbf{S}_{VV_{f_2}} \end{bmatrix}$$

The corresponding 3-D MCA Pauli scattering target vectors \mathbf{K}_{f_1} and \mathbf{K}_{f_2} are given by:

$$\mathbf{K}_{f_1} = \begin{bmatrix} \mathbf{S}_{HH_{f_1}} + \mathbf{S}_{VV_{f_1}} \\ \mathbf{S}_{HH_{f_1}} - \mathbf{S}_{VV_{f_1}} \\ 2\mathbf{S}_{HV_{f_1}} \end{bmatrix} \quad (9)$$

and

$$\mathbf{K}_{f_2} = \begin{bmatrix} \mathbf{S}_{HH_{f_2}} + \mathbf{S}_{VV_{f_2}} \\ \mathbf{S}_{HH_{f_2}} - \mathbf{S}_{VV_{f_2}} \\ 2\mathbf{S}_{HV_{f_2}} \end{bmatrix}$$

The six-element MCA-PolInSAR scattering vector is given by $\mathbf{T}_6 = [\mathbf{K}_{f_1} \mathbf{K}_{f_2}]^\dagger$. The \mathbf{T}_6 coherency matrix has the following configuration:

$$\mathbf{T}_6 = \begin{bmatrix} \mathbf{T}_{11} & \Omega_{12} \\ \Omega_{12}^\dagger & \mathbf{T}_{22} \end{bmatrix} \quad (10)$$

The parameter Ω_{12} of the MCA – \mathbf{T}_6 matrix is equal to: $\Omega_{12} = \frac{1}{n} \sum \mathbf{K}_{f_1} \mathbf{K}_{f_2}^\dagger$. The infra-chromatic cross-correlation matrix Ω_{12} has complex elements which is computed the following complex infra-chromatic coherence:

$$\gamma = \frac{\langle \mathbf{K}_{f_1} \mathbf{K}_{f_2}^\dagger \rangle}{\sqrt{\langle \mathbf{K}_{f_1} \mathbf{K}_{f_1}^\dagger \rangle \times \langle \mathbf{K}_{f_2} \mathbf{K}_{f_2}^\dagger \rangle}}. \quad (11)$$

The magnitude of the complex matrix γ indicates the correlation degree existing between the two infra-chromatic images. The argument of the coherence indicate the interference degree between the frequencies selected according to Figure 1(a) and (b). The thesis of the author is that more information can be extrapolated by the MCA. According to (Ferretti et al. 2001), considering two SAR observations spaced by a certain space-time baseline, the total interferometric coherence is given by the following relation:

$$\gamma = \gamma_{\text{SNR}} \gamma_{\text{quant}} \gamma_{\text{amb}} \gamma_{\text{geo}} \gamma_{\text{az}} \gamma_{\text{rg}} \gamma_{\text{vol}} \gamma_{\text{temp}} \gamma_{\text{proc}} \gamma_{\text{pol}}. \quad (12)$$

Each term indicates a decorrelation level related to the following physical parameters:

- (1) **SNR**: is related to the thermal noise level generated by the transmitted amplifiers and the low-noise amplifier locate on the receiver chain;
- (2) **quant**: is the quantization noise. the most of the SARs are equipped with the block adaptive quantization (BAQ) which is deputed to reduce the sensitivity level of the raw data. a BAQ(n, m) reduced in m bits of quantization level. This data reduction produced decorrelation.
- (3) **amb**: these decorrelation effects are related to the radar ambiguities;
- (4) **geo**: geometric decorrelation due to baseline and squint but also by other orbital or flight path noises;
- (5) **vol**: Volume decorrelation generated by electromagnetic penetration effects;
- (6) **temp**: temporal decorrelation.
- (7) **proc**: processing decorrelation.
- (8) **pol**: polarimetric effects.
- (9) **rg**: decorrelation generated by range compression.
- (10) **az**: decorrelation generated by azimuth compression.

The thesis of the author is also that the item number 3 referring to the **geo** parameter is incomplete and can be analyzed in a more precise manner. A SAR acquisition, during the Doppler integration process the sensor collects electromagnetic echoes while is moving. this procedure can be split in several sub-apertures so to estimate different Doppler infra-chromatic coherence maps. The parameter **geo** can so be considered also on the single acquisition. This “**fast-geo**” approach contribute to decorrelate the MCA-PolInSAR study cases considered in this paper. The dependency of the MCA-PolInSAR coherence on the polarization formed by \mathbf{K}_{f_1} and \mathbf{K}_{f_2} leads to consider the question of which combination of polarization

yields the highest coherence. In (Ferro-Famil et al. 2001) and (Ferro-Famil et al. 2006) authors proposed a method that maximizes a complex Lagrangian function and estimating the following infra-chromatic optimized complex coherencies that have been estimated also using the MCA approach.

$$1 \leq |\text{MCA}\gamma_{\text{opt}_1}| \leq |\text{MCA}\gamma_{\text{opt}_2}| \leq |\text{MCA}\gamma_{\text{opt}_3}|. \quad (13)$$

In Ferro-Famil et al. (2001) and Ferro-Famil et al. (2006) a classification distance based on the spatial baseline interferometric coherence has been developed and the author is applying the same theory developed in Ferro-Famil et al. (2001) and Ferro-Famil et al. (2006) replacing the spatial baseline interferometric coherence based on PollnSAR with the optimum infra-chromatic coherencies based on the MCA-PollnSAR. The MCA infra-chromatic distance will so have the following configuration:

$$\begin{aligned} d(\mathbf{R}) = n \ln(|\mathbf{P}_m - \mathbf{I}_3|) - \\ + \ln(\mathbf{F}_1(n, n, 3, \mathbf{P}_m, \mathbf{R}_{\text{MCA}})) \end{aligned} \quad (14)$$

In (12) n is the number of the independent looks, the parameter $\mathbf{F}_1(n, n, 3, \mathbf{P}_m)$ is an hyper-geometric function, the parameter \mathbf{I}_3 is a 3×3 unity matrix and the parameter $\mathbf{P}_m = E[\mathbf{R}|\omega_m]$ is the class centre of the class ω_m with $m = 3$ classes. The parameter \mathbf{R}_{MCA} is defined by the following matrix:

$$\mathbf{R}_{\text{MCA}} = \begin{bmatrix} \mathbf{J}_1 & 0 & 0 \\ 0 & \mathbf{J}_2 & 0 \\ 0 & 0 & \mathbf{J}_3 \end{bmatrix} \quad (15)$$

where the diagonal parameters $\mathbf{J}_1 = |\text{MCA}\gamma_{\text{opt}_1}|^2$, $\mathbf{J}_2 = |\text{MCA}\gamma_{\text{opt}_2}|^2$ and $\mathbf{J}_3 = |\text{MCA}\gamma_{\text{opt}_3}|^2$. The MCA-PollnSAR segmentation procedure is depicted in Figure 33 and uses the complex 6×6 \mathbf{T}_6 MCA-PollnSAR matrix and the MCA optimized infra-chromatic coherences $\mathbf{J}_i, i = 1, 2, 3$.

4. Experimental results

Experimental results consist of two study cases representing the polarimetric classification of one dataset acquired by the COSMO-SkyMed (CSK) satellite system over the city of Tucson (USA) and one airborne data-set acquired by the Unmanned Aerial Vehicle Synthetic Aperture Radar (UAVSAR) sensor over the city of Hayward (USA). The CSK satellite system observed data at 9.6 GHz of central frequency in 90 MHz of the electromagnetic band which allows 3 m of resolution in range. The Doppler bandwidth is 2.63 kHz which allows same resolution in azimuth and 40 km of the swath in range. The UAVSAR sensor transmits electromagnetic bursts at 1.26 GHz and 80 MHz of chirp bandwidth which allows 3.5 m of range resolution and nearly 5 m of azimuth resolution on a swath of 16 km in range. Figure 3(a) represents the full-polarimetric satellite result and Figure 3(b) is the equivalent full polarimetric airborne result. The pictures has been focused using the entire Doppler band and the full-polarimetric capabilities shows a good general separation of the HH+VV (blue, single-bounce scattering event), HH-VV (red, double-bounce scattering event) and HV+VH (green, volume scattering event) polarization channels. Unfortunately, using the full resolution and only one SAR image make the volume indetermination effect difficult to be solved. observing the pictures, in both

satellite and airborne polarimetric results, blocks of buildings are detected in the green polarimetric channel. Figure 33 shows the scheme of the algorithm used to perform the MCA-PollnSAR urban classification. The procedure starts with a single raw SAR dataset (block number 1). The output is split into blocks 2 and 3 consisting of two filters and a focusing procedure sub-chain. Stages number 2 and 3 generates the master-F1 and the slave-F2 SLC SAR images, according to the frequency allocation plane showed in Figure 1(b). Stage number three generate the \mathbf{T}_6 matrix which output is given as input to stages number 5 and 6. Stage 5 performs the estimate of the optimized infra-chromatic coherences $MCA_{i=1,2,3}$ according to Ferro-Famil et al. (2001) and Ferro-Famil et al. (2006) and stage 6 performs the unsupervised Wishart classification according to the parameters set by the block number 7. For example, a parameter that can be set is the number of independent looks n . The stage number 8 represents the output of the MCA-PollnSAR classification results.

4.1. Classification algorithms

Figure 33, block 6 shows that MCA-PollnSAR use the unsupervised maximum likelihood Wishart classification for producing de-oriented results. The algorithm uses the following statistical distribution:

$$\begin{aligned} \mathbf{P}(\mathbf{T}|\boldsymbol{\Gamma}_m) &= \frac{[\langle \mathbf{T}_6 \rangle]^{L-p} \exp\left(-([\boldsymbol{\Gamma}^{-1}] \langle \mathbf{T}_6 \rangle)^T\right)}{\mathbf{K}(L,p)[\boldsymbol{\Gamma}_m]^L} = \\ &= \mathbf{W}(L, [\boldsymbol{\Gamma}_m]) \end{aligned} \quad (16)$$

where

$$\mathbf{K}(L,p) = \frac{\pi^{\frac{p(p-1)}{2}}}{\mathbf{L}^p} (\{\boldsymbol{\Gamma}(L)\} \dots \{\boldsymbol{\Gamma}(L-p+1)\}). \quad (17)$$

In (16) the symbol T represent the matrix transpose, the parameter $\boldsymbol{\Gamma}_m$ represents the cluster centre of the class m and in (16) and (17) the parameter L represents the number of independent looks. The parameters $(\{\boldsymbol{\Gamma}(L)\} \dots \{\boldsymbol{\Gamma}(L-p+1)\})$ are a series of complex gamma functions and the symbol p represents the polarimetric dimension which in this case is equal to 6.

4.2. Study case one results

Figures 4, 5 and 6(a) represents the magnitude of the HH+VV polarimetric channel optimized infra-chromatic coherences estimated between the master focused at frequency F1 and the slave focused at frequency F2. Figures 4, 5 and 6(b) represents the phase of the same (F1-F2) optimized infra-chromatic coherences. The values of the infra-chromatic Doppler frequencies are selected according to the frequency allocation table reported in Figure 1. Figure 1(a) is the frequency allocation plane used to generate the master and the slave of the COSMO-SkyMed data set. The master image is focused from 0 to 4 kHz and the slave image occupies the rest of the Doppler band (3–7 kHz). Figure 1(b) is the frequency allocation plane of the airborne data-set. For this airborne case the master is focused from 0 to 3 kHz and the slave from 2 to 5 kHz. The author designed for the study-case number one a frequency baseline set to 2 kHz and for

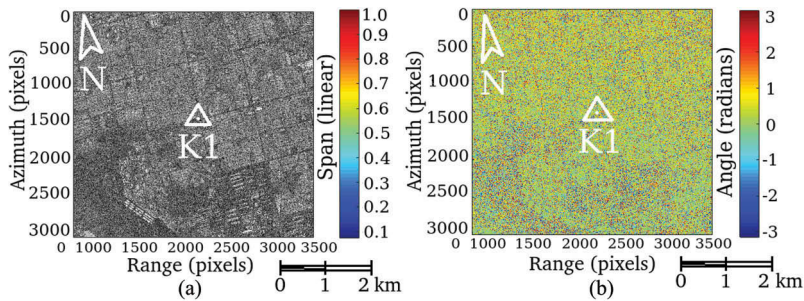


Figure 4. Infra-chromatic coherence. (a): magnitude. (b): phase.

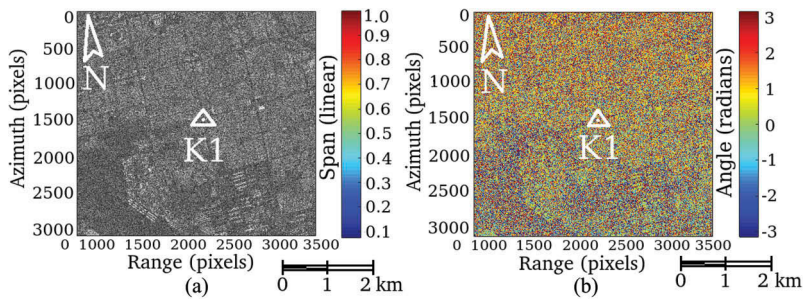


Figure 5. Infra-chromatic coherence. (a): magnitude. (b): phase.

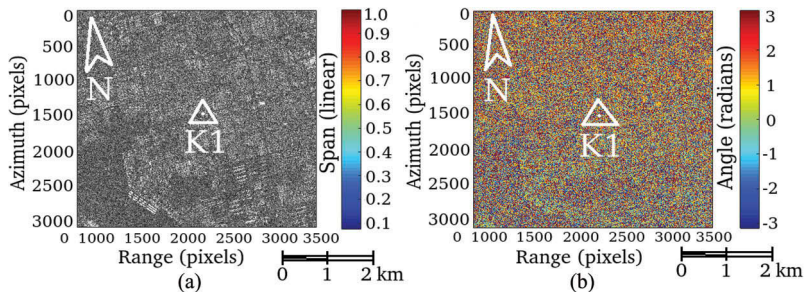


Figure 6. Infra-chromatic coherence. (a): magnitude. (b): phase.

the study-case number two the frequency baseline is set to 1 kHz. This separation was found sufficient to estimate a useful infra-chromatic coherence. Figure 7(a) is the red-green-blue (RGB) of the magnitude infra-chromatic coherences. Figure 7(b) is instead the RGB phase. Figure 8(a,b,c) shows the entropy-anisotropy-alpha unsupervised, Wishart supervised and MCA-PollnSAR classification outputs respectively. Result depicted in Figure 8(b) is taken to be a reference for discussing the MCA-PollnSAR classification performance. The results are estimated using all the available Doppler band. The performance of all the proposed results are commented in the discussion section. Figure 10(a) is the double-bounce cluster of the entropy-anisotropy-alpha supervised classification and Figure 10(b) is its alter-ego using the unsupervised Wishart classification. Detailed results are depicted in Figure 11(a,b,c) where in Figure 11(a) is the unsupervised classification cluster, Figure 11(b) is the Wishart supervised classification

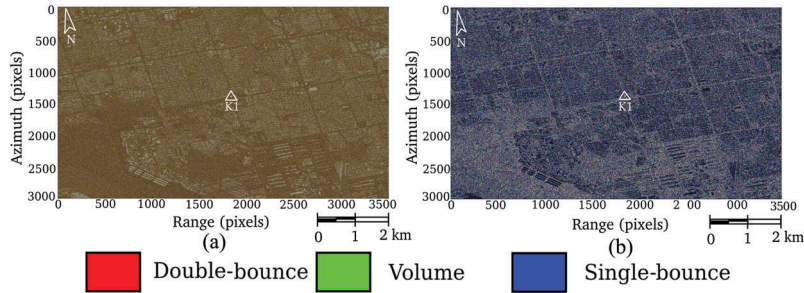


Figure 7. Infra-chromatic coherence RGB. (a): magnitude. (b): phase.

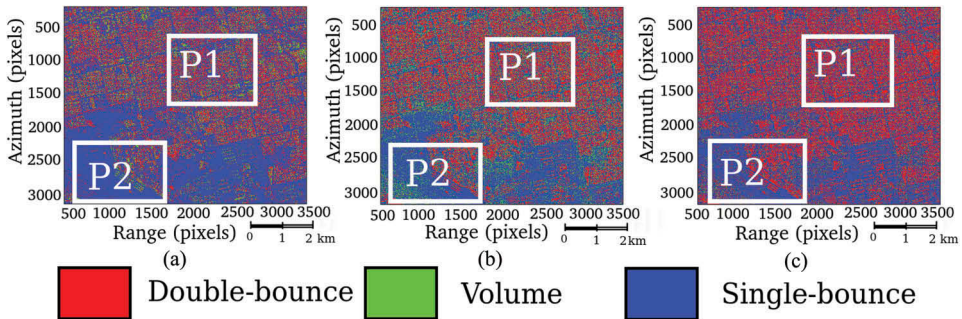


Figure 8. Classification results: the red channel is the (HH-VV) double-bounce, the blue channel is the (HH+VV) single bounce and the green channel is the volume. (a): unsupervised classification. (b): supervised classification. (c): MCA-PollnSAR unsupervised classification.

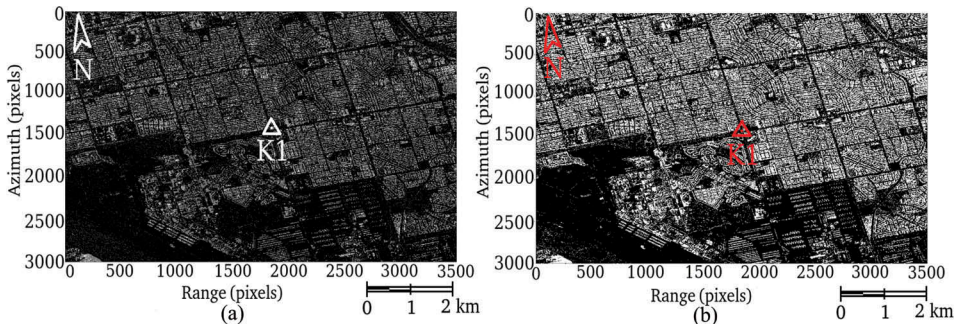


Figure 9. Double-bounce clustering. (a): unsupervised classification. (b): supervised classification.

result and [Figure 11\(c\)](#) is the MCA-PollnSAR result. All the sub-captures are extrapolated by the white box P1 of [Figure 8\(a,b,c\)](#). [Figure 12\(a,b\)](#) are the wishart supervised and the MCA-PollnSAR classification results extrapolated by the white box P2 of [Figure 8\(a,b,c\)](#). Result plotted by the [Figure 12\(b\)](#) is impressively more detailed respect to the supervised result ([Figure 12\(a\)](#)). The MCA-PollnSAR classification allows fine detection of the airport runways respect to the supervised result. The points are geolocated at the following coordinates: $K_1: 32^\circ 11' 31.7184'' N, 110^\circ 51' 28.9584'' W$; $K_3: 32^\circ 11' 1.212'' N, 110^\circ 53' 28.2948'' W$.

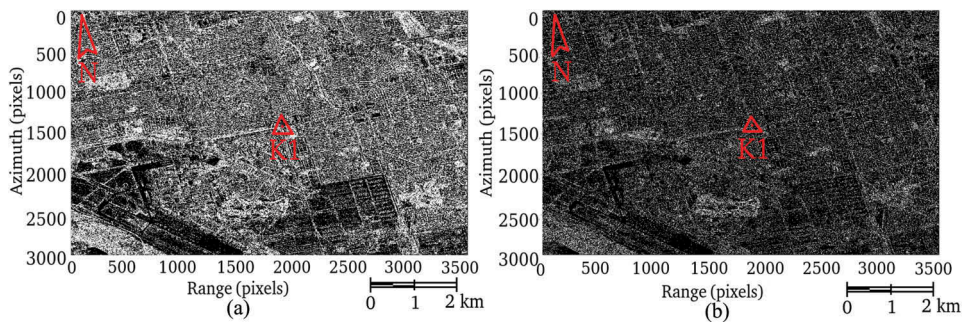


Figure 10. Volume clustering. (a): unsupervised classification. (b): supervised classification.

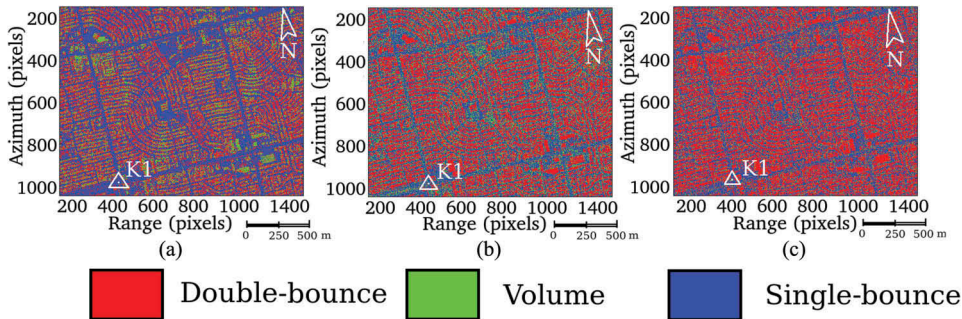


Figure 11. Classification results: the red channel is the (HH-VV) doublebounce, the blue channel is the (HH+VV) single bounce and the green channel is the volume. (a): unsupervised classification. (b): supervised classification. (c): MCA-PollnSAR unsupervised classification.

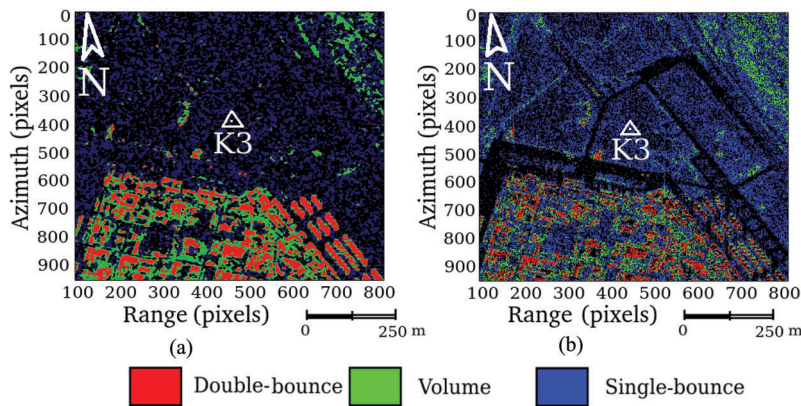


Figure 12. Classification results. (a): Supervised classification full band fullpol. (b): MCA-PollnSAR classification.

4.3. Study case two results

The case of study number two is referred to all the classification results estimated considering one UAVSAR data set where the full-polarimetric RGB image is depicted in Figure 3(b). Figures 13, 14 and 15(a) represents the magnitude of the HH+VV

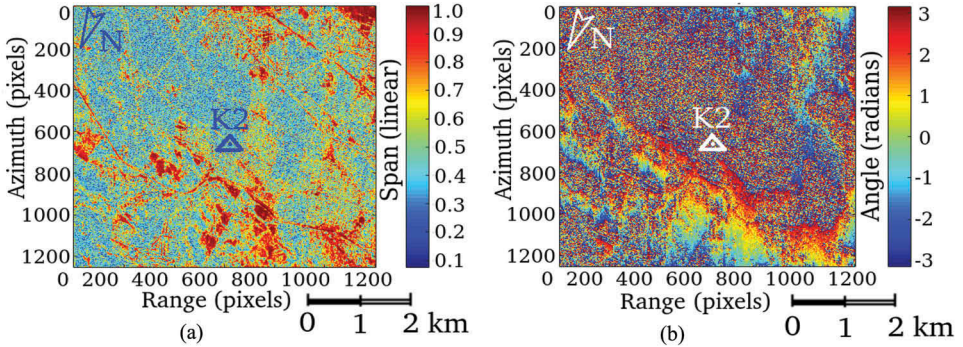


Figure 13. UAVSAR study case infra-chromatic optimum coherence.(a): Magnitude. (b): Phase.

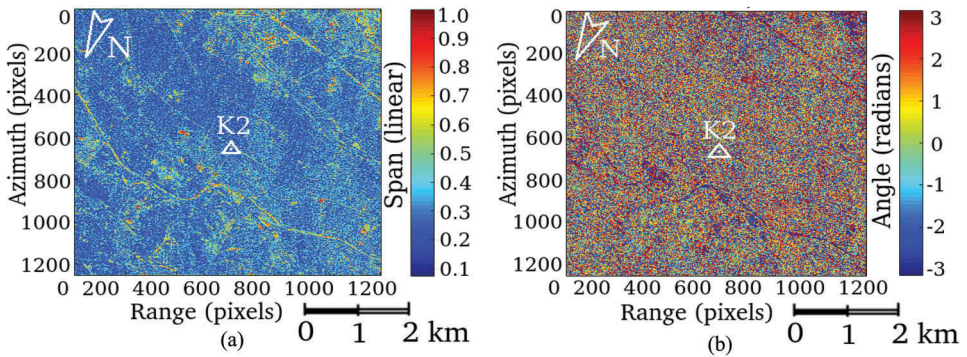


Figure 14. UAVSAR study case infra-chromatic optimum coherence.(a): Magnitude. (b): Phase.

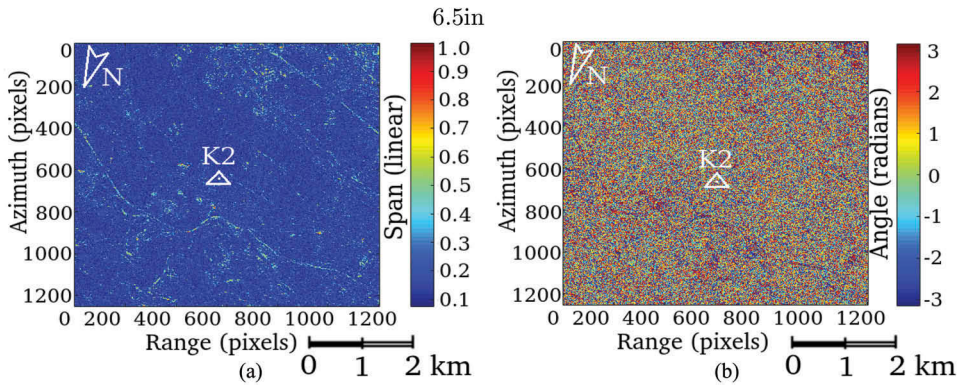


Figure 15. UAVSAR study case infra-chromatic optimum coherence.(a): Magnitude. (b): Phase.

polarimetric channel optimized infra-chromatic coherences estimated between the master focused at frequency F1 and the slave focused at frequency F2. [Figures 13, 14](#) and [15](#) (a) and (b) represents the phase of the same (F1-F2) optimized infra-chromatic coherences. The values of the infra-chromatic Doppler frequencies are selected according to

the frequency allocation table reported in Figure 1(b), the frequency allocation plane is used to generate the master and slave infra-chromatic data useful to estimate the coherence. The master image is focused using the maximum chirp band and from 0 Hz to 3 kHz in Doppler band. The slave image occupies the same entire chirp in range and the other side of the available Doppler band from 2 kHz to 5 kHz. The author designed for the study-case number one and two a frequency baseline set to $B_1 = B_2 = 2$ kHz. This separation was found sufficient to estimate a useful infra-chromatic coherence. Figure 16(a) is the RGB of the magnitude infra-chromatic coherences. Figure 16(b) is instead the RGB built by the phase information. Figure 17(a,b,c) shows the entropy-anisotropy-alpha unsupervised, Wishart supervised and MCA-PollnSAR classification outputs respectively. Result depicted in Figure 17(b) is taken to be a reference for discussing the MCA-PollnSAR classification performance. The results are estimated using all the available Doppler band. The performance of all the proposed results are commented in the discussion section. Detailed results are depicted in Figure 18(a,b,c) where in Figure 18(a) is the unsupervised classification cluster, Figure 18(b) is the Wishart supervised classification result and Figure 18(c) is the MCA-PollnSAR result. All the sub-captures are extrapolated by the white box P1, P2 and P3 of Figure 17(a,b,c). Figures 19, 20 and 24(a, b,c) are the entropy-anisotropy-alpha unsupervised, Wishart supervised and MCA-PollnSAR classification outputs respectively where results are extrapolated grabbing data from the white boxes P1, P2 and P3 of Figure 17(a,b,c). The points are geolocated

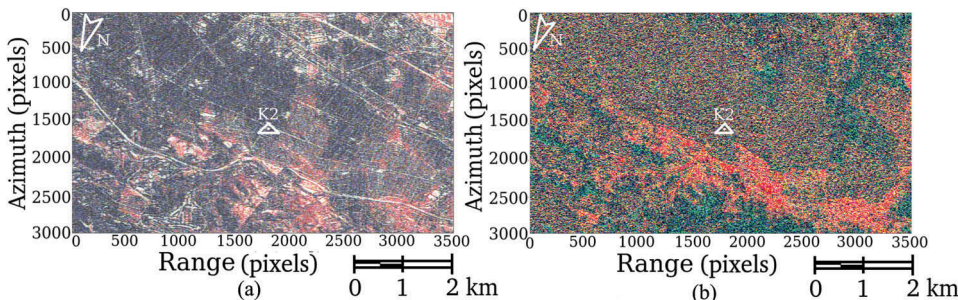


Figure 16. Full polarimetric SAR images. The red channel is generated by the HH-VV double-bounce. The blue channel is populated by the HH+VV single-bounce.

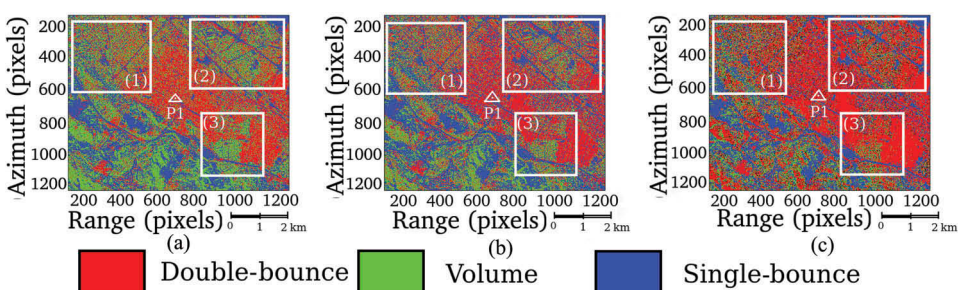


Figure 17. PolSAR classification results. (a): Wishart unsupervised classification. (b): Wishart supervised classification. (c): MCA-PollnSAR unsupervised classification.

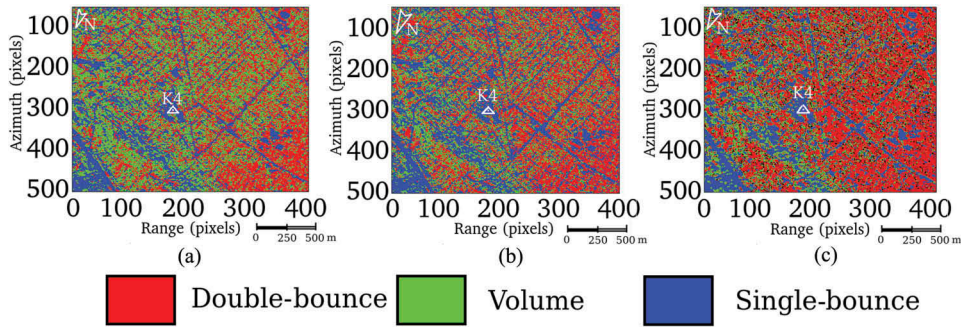


Figure 18. Particular of the PolSAR classification results of Figure 17: supervised classification. (a): Wishart unsupervised classification. (b): Wishart supervised classification. (c): MCA-PollnSAR unsupervised classification.

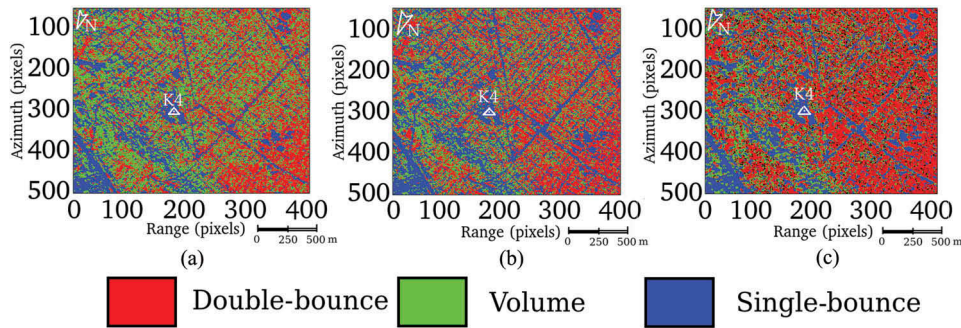


Figure 19. Particular of the PolSAR classification results of Figure 17: supervised classification. (a): Wishart unsupervised classification. (b): Wishart supervised classification. (c): MCA-PollnSAR unsupervised classification.

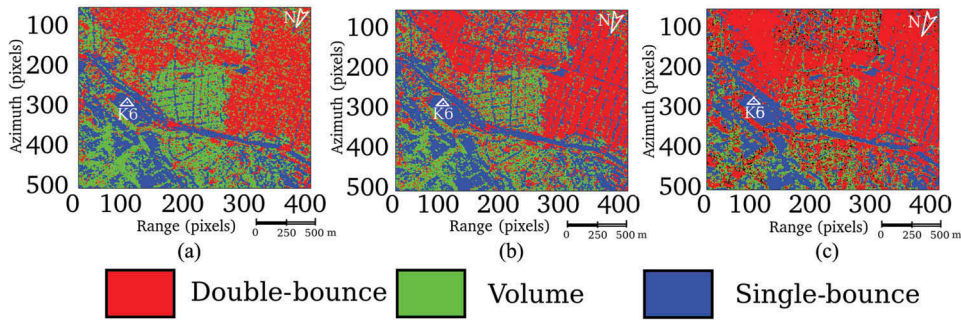


Figure 20. Particular of the PolSAR classification results of Figure 17: supervised classification. (a): Wishart unsupervised classification. (b): Wishart supervised classification. (c): MCA-PollnSAR unsupervised classification.

at the following coordinates: K_2 : $37^{\circ} 44' 54.942''$ N, $122^{\circ} 9' 42.3792''$ W; K_4 : $37^{\circ} 46' 19.6212''$ N, $122^{\circ} 46' 19.6212''$ W; K_5 : $37^{\circ} 44' 27.5244''$ N, $122^{\circ} 46' 48.9612''$ W; K_6 : $37^{\circ} 44' 27.0348''$ N, $122^{\circ} 08' 32.6580''$ W; K_7 : $37^{\circ} 43' 56.4816''$ N, $122^{\circ} 10' 59.8872''$ W; K_8 : $37^{\circ} 45' 53.2620''$ N, $122^{\circ} 10' 55.6140''$ W; K_7 : $37^{\circ} 43' 33.6936''$ N, $122^{\circ} 08' 48.6816''$ W.

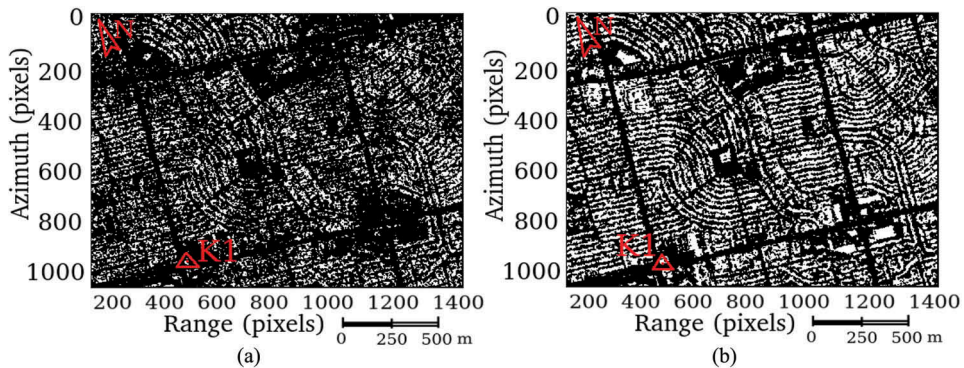


Figure 21. Correct decision map. (a): Unsupervised classification. (b): MCA-PollnSAR classification.

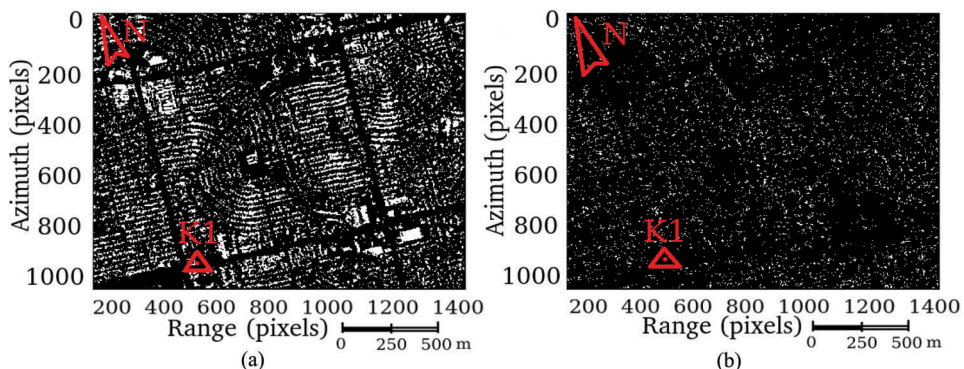


Figure 22. Mis-decision map. (a): Unsupervised classification. (b): MCA-PollnSAR classification.

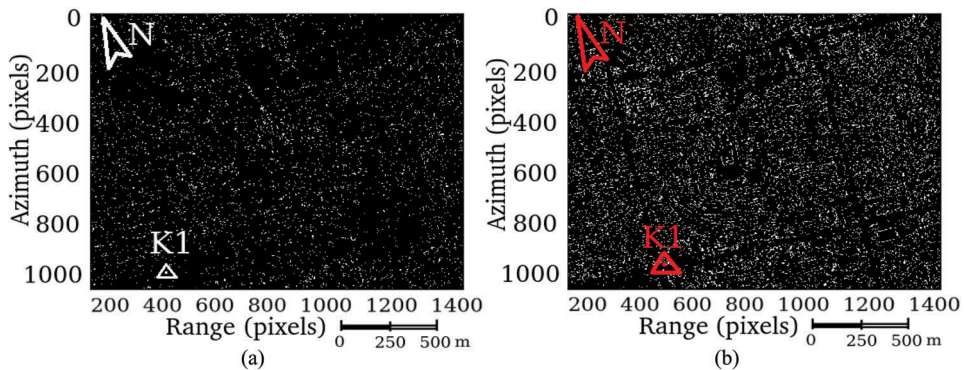


Figure 23. False alarm map. (a): Unsupervised classification. (b): MCA-PollnSAR classification.

5. Discussion

In this section, all the classification results are analyzed. From the analysis of different polarimetric and Doppler multi-chromatic contribution, it is possible to classify the MCA-PollnSAR images showing clear discrimination between different areas. The performances

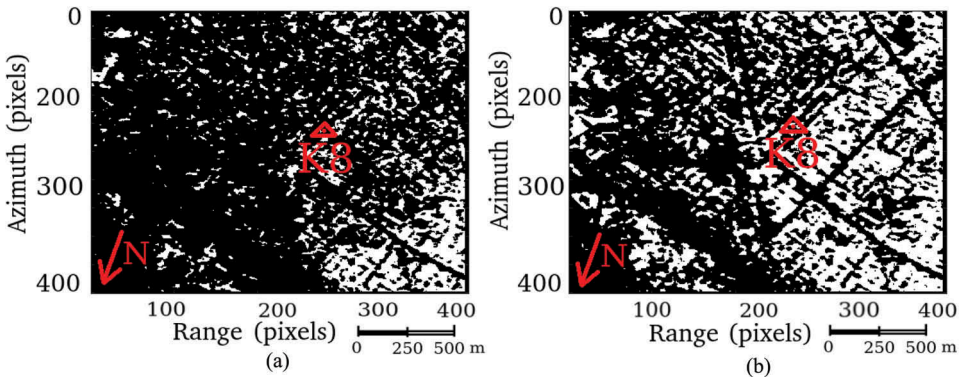


Figure 24. Correct decision map. (a): Unsupervised classification. (b): MCA-PollnSAR classification.

are observed comparing the classification methods explained in (Ferro-Famil et al. 2001) respect to the supervised method explained in (Lee, Grunes, and Pottier 2001). Results estimated by the MCA-PollnSAR classification process are compared with the other two methods, the unsupervised one (Ferro-Famil et al. 2001) and the supervised one (Lee, Grunes, and Pottier 2001). It has been found that the MCA-PollnSAR process is very robust and indicated to perform the deorientation of urban scattering mechanisms.

5.1. Study case one performance discussion

In Figure 11(a,b,c) the red channel is the double-bounce scattering, the green channel is the volume and the blue channel in the single-bounce polarimetric scattering event decision. The result depicted in Figure 11(b) is clearly better if compared to the one depicted in Figure 11(a). The high performance is given because of using a supervision strategy for classification. The unsupervised output is characterized by a massive amount of mis-classification due to the volume oriented indetermination. Considering the robustness given by the supervision, the author considers this result which is collected in Figure 11(b) to be the reference for measuring the performance of all other MCA-PollnSAR classifications. Figure 11(c) is the MCA-PollnSAR unsupervised classification results, found to be very similar to the supervised map. Figure 9(a,b) shows only the red channel (double-bounce) decisions of Figure 8 where Figure 9(a) are the double-bounce decisions of the unsupervised entropy-anisotropy-alpha Wishart classification (Figures 8(a)) and 9(b) are the supervised decisions (Figure 8(b)). The supervised classification method gives absolutely more double-bounce decisions respect to the unsupervised. Figure 10 shows the green channel decisions of the results showed in Figure 8 (a,b). Figure 10(a) are the volume decisions of the unsupervised entropy-anisotropy-alpha Wishart classification and Figure 10(b) are the supervised decisions. It is possible to note that the most of the double-bounce decisions of Figure 9(a) are mismatched to the green channel of Figure 10(a). Figure 11(b) shows the RGB supervised classification map and Figure 11(c) is the RGB unsupervised MCA-PollnSAR classification result. In Figure 11 (c) buildings, vegetation and streets are plotted more precisely with respect to the objects classified using the PolSAR approach (Figure 11(a,b)). Observing Figure 11(c) it is also possible to appreciate greater precision in classification accuracy where the MCA-

Table 1. MCA-PollnSAR versus unsupervised classification performance.

Method	Sensor	Area	Figures	Hit	Miss	FA	CR
MCA-PollnSAR	CSK	P1	(21–23)(b)	0.337	0.0446	0.035	0.582
Unsupervised	CSK	P1	(21–23)(a)	0.203	0.1789	0.089	0.528

PollnSAR approach has been applied. A higher classification accuracy is detected by the increasing of precision in the description of objects around their canonical scattering mechanisms which are more precisely separated. In each class estimated by the MCA-PollnSAR approach, new details are detected which are not represented using the standard PolSAR approach. In this new case, the buildings are correctly classified in the double-bounce polarimetric red channel. Results in [Figure 11\(c\)](#) confirms that the unsupervised PolSAR classification method, that uses the MCA-PollnSAR sub-apertures, is sufficiently robust to resolve the volume oriented indetermination and reaching the same precision of the supervised algorithm. [Figure 12\(a,b\)](#) shows an airport where the taxiways are visible only on the MCA-PollnSAR classification result ([Figure 12\(b\)](#)) and in [Figure 12\(a\)](#) are not visible. [Figures 21,22](#) and [23](#) are correct-decision, mis-decision and the false-alarm-decision maps of the unsupervised classification of [Figure 8\(a\)](#) and [\(c\)](#) respect to the supervised classification result of [Figure 8\(b\)](#) which has been used as the ground-truth (the so called "synthetic"). Performance of the MCA-PollnSAR classification method are reported in [Table 1](#).

Table number one represents the classification performances of the case of study number one. [Figure 21\(a\)](#) is the correct-decision map of the unsupervised classification method and [Figure 21\(b\)](#) is the correct-decision map of the unsupervised MCA-PollnSAR. According to [Table 1](#), the MCA-PollnSAR process gives higher hit probability with respect to the unsupervised process. [Figure 22\(a\)](#) is the false alarm (FA) map of the unsupervised classification method and [Figure 22\(b\)](#) is the FA classification map using the unsupervised MCA-PollnSAR. According to [Table 1](#), the MCA-PollnSAR method gives lower FA probability with respect to the unsupervised process. [Figure 22\(a\)](#) is the mis-decision map of the unsupervised classification process and [Figure 22\(b\)](#) is the mis-decision classification map using the unsupervised MCA-PollnSAR. According to [Table 1](#), the MCA-PollnSAR method gives lower mis-decision probability with respect to the unsupervised method. In conclusion, the MCA-PollnSAR according to this first case of study gives a higher performance which has better performances with respect to the standard unsupervised methods. Performance of the MCA-PollnSAR classification process is reported in [Table 1](#).

5.2. Study case two performance discussion

The UAVSAR airborne sensor has high-performance and quality full polarimetric capabilities. The raw data is sampled and digitalized on 12 bits respect to the raw data produced by the satellite system COSMO-SkyMed which is quantized using only 3 bits in precision. This inconvenience happens because the radar echoes returning to the receiver are compressed using the unadaptive BAQ(8,3) scheme. However, the table number two contains the classification performances data concerning the case of study number two. [Figures 24, 27](#) and [30\(a\)](#) are the correct-decision maps of the unsupervised

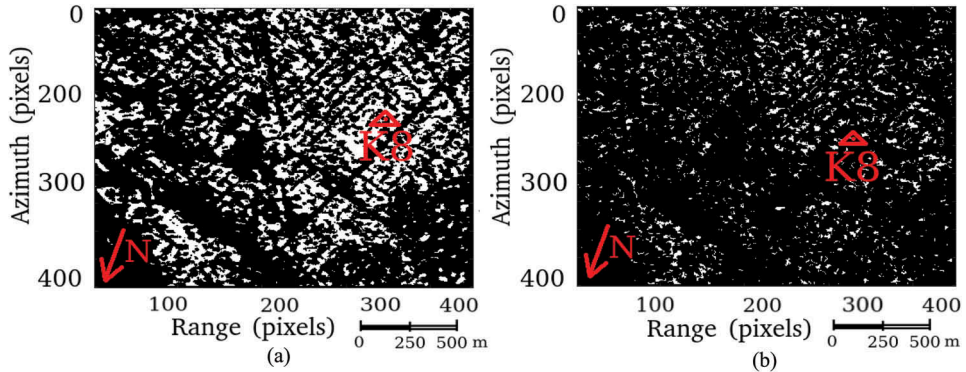


Figure 25. Mis-decision map. (a): Unsupervised classification. (b): MCA-PollnSAR classification.

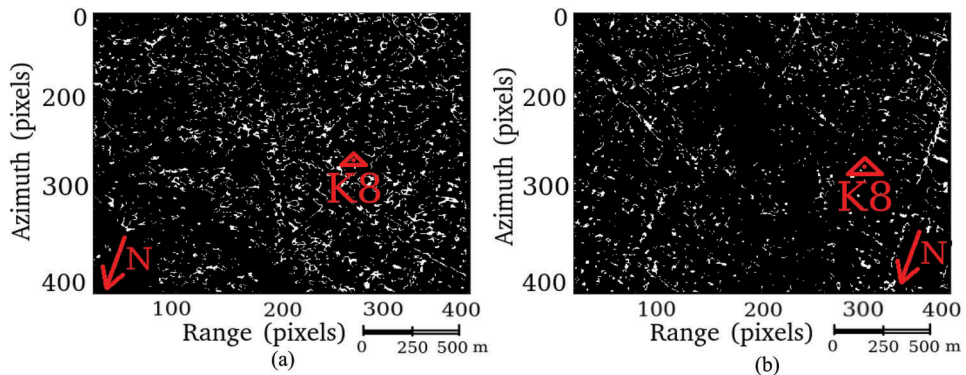


Figure 26. False alarm decision map. (a): Unsupervised classification. (b): MCA-PollnSAR classification.

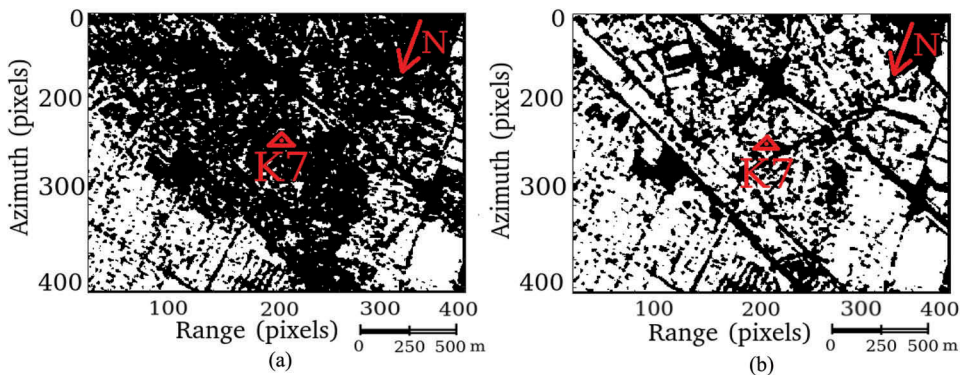


Figure 27. Correct decision map. (a): Unsupervised classification. (b): MCA-PollnSAR classification.

classification method of Figure 18(a). Figures 24, 27 and 30(b) are the correct-decision maps of the unsupervised MCA-PollnSAR of Figure 18(c). Figures 26, 29 and 32(a) are the FA maps of the unsupervised classification process and Figure 19(a). Figures 26, 29 and

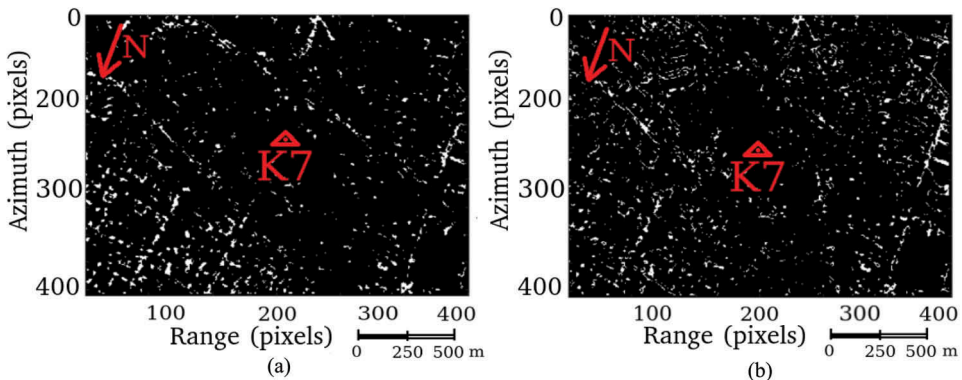


Figure 28. Mis-decision map. (a): Unsupervised classification. (b): MCA-PollnSAR classification.

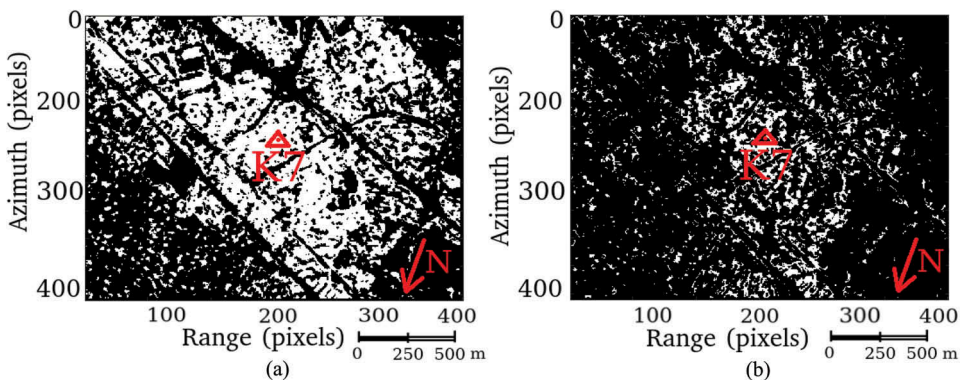


Figure 29. False alarm decision map. (a): Unsupervised classification. (b): MCA-PollnSAR classification.

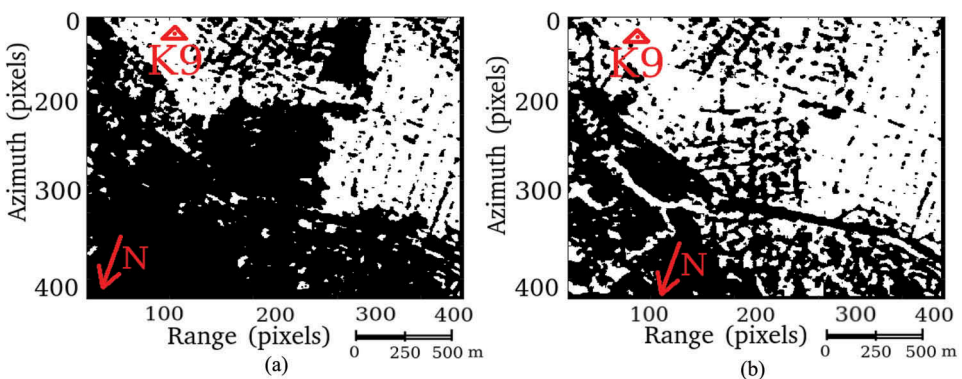


Figure 30. Correct decision map. (a): Unsupervised classification. (b): MCA-PollnSAR classification.

32(b) are the FA maps of the unsupervised classification method and Figure 19(c). Figures 25, 28 and 31(a) are the FA maps of the unsupervised classification process of Figure 20(a). Figures 25, 28 and 31(b) are the FA maps of the unsupervised classification

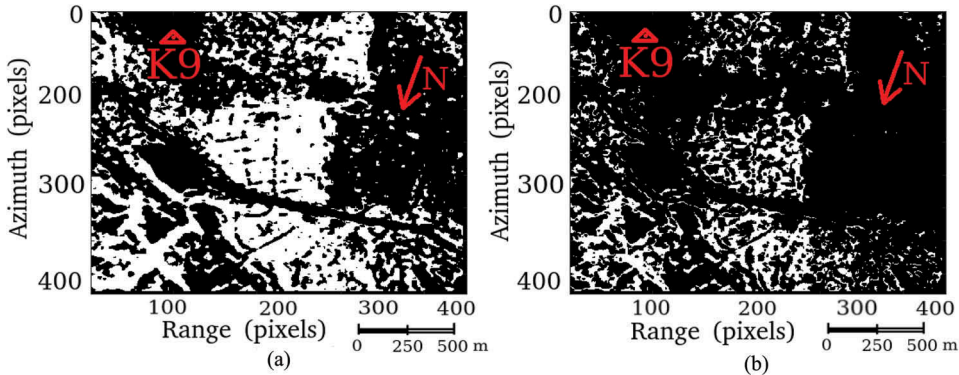


Figure 31. Mis-decision map. (a): Unsupervised classification. (b): MCA-PollnSAR classification.

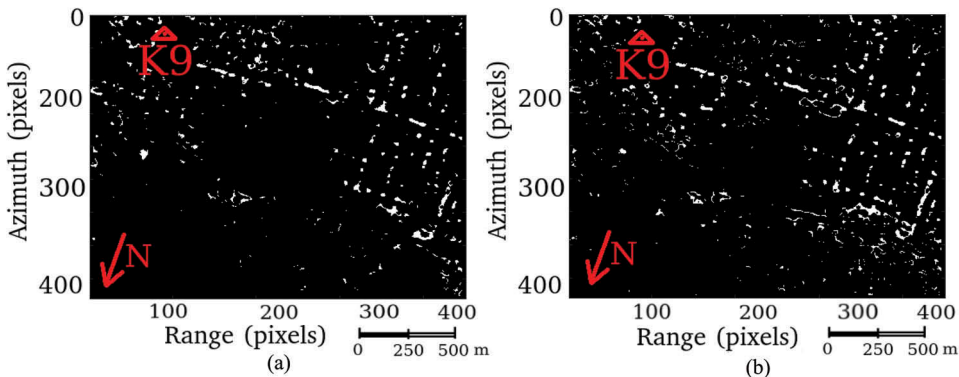


Figure 32. False alarm decision map. (a): Unsupervised classification. (b): MCA-PollnSAR classification.

method of Figure 20(c). According to Table 2 the MCA-PollnSAR process gives higher hit probability with respect to the unsupervised method. According to Table 2 the MCA-PollnSAR method gives lower FA probability with respect to the unsupervised process. Figure 22(a) is the mis-decision map of the unsupervised classification process and Figure 22(b) is the mis-decision classification map using the unsupervised MCA-PollnSAR. According to Table 1 the MCA-PollnSAR method gives lower mis-decision probability respect to the unsupervised process. In conclusion, the MCA-PollnSAR according to second-case of study which performances are reported in Table 2, gives higher performance respect to the standard unsupervised methods. In particular the MCA-PollnSAR gives less mis-probability with respect to the unsupervised process. The correct classification probability of the MCA-PollnSAR is enormously greater if compared to the unsupervised strategy. The price to pay is that the MCA-PollnSAR process returns a small increase of the FA probability and a small decrease of the rejection probability respect to the unsupervised strategy.

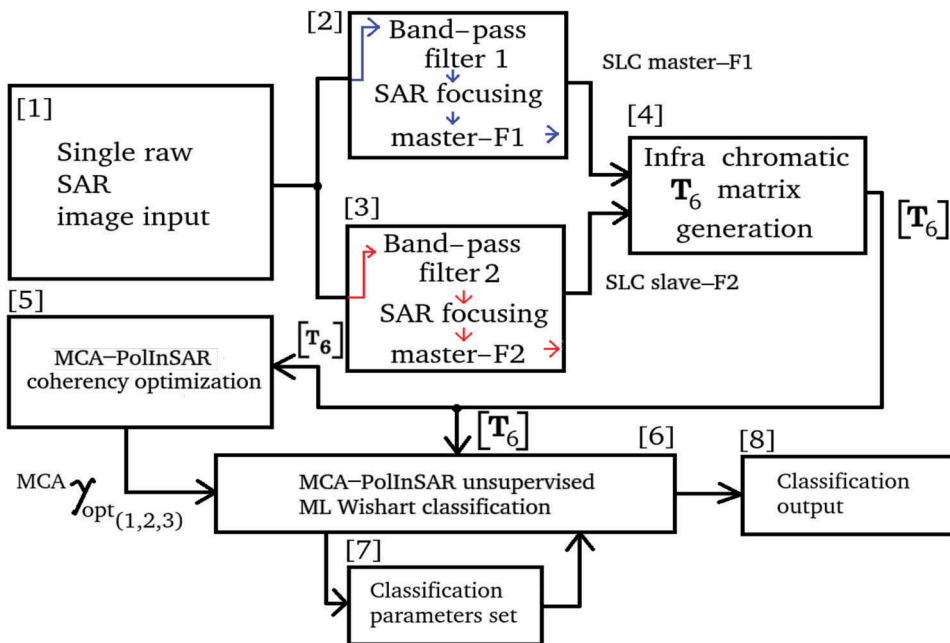


Figure 33. Full polarimetric SAR images. The red channel is generated by the HH-VV double-bounce. The blue channel is populated by the HH+VV single-bounce.

Table 2. MCA-PolInSAR versus unsupervised classification performance.

Method	Sensor	Area	Figures	Hit	Mis	FA	CR
MCA-PolInSAR	UAVSAR	P1	(24–26)(b)	0.542	0.152	0.0344	0.271
Unsupervised	UAVSAR	P1	(24–26)(a)	0.327	0.367	0.0269	0.279
MCA-PolInSAR	UAVSAR	P2	(27–29)(b)	0.582	0.116	0.0462	0.255
Unsupervised	UAVSAR	P2	(27–29)(a)	0.305	0.393	0.0423	0.259
MCA-PolInSAR	UAVSAR	P3	(30–32)(b)	0.349	0.068	0.0704	0.512
Unsupervised	UAVSAR	P3	(30–32)(a)	0.165	0.251	0.0564	0.527

6. Conclusions

In this paper, the MCA analysis of full-polarimetric SAR data has been proposed. The spectral diversity was generated to produce sufficiently independent information to appreciate the unsupervised classification of scattering events. The MCA-PolInSAR configuration is based on the Doppler sub-apertures SAR refocusing of the airborne full-polarimetric dataset. The spectral diversity existing between the master and the slave sub-products extrapolated from only one SAR image was found sufficient to estimate a set of infra-chromatic complex coherencies. The estimation of this infra-chromatic coherencies were performed between all the polarization channels combinations. The obtained results were used like additional information useful to delete the volume-oriented scattering indetermination procured by misalignment of buildings with respect to the radar-target slant-range. The innovation proposed in this paper, bases its computational core on the processing of only one full polarimetric SAR image, in the HH, HV, VH and HH channels. Until now, similar results were obtained by processing two PolInSAR full polarimetric images, acquired on a spatial baseline.

SAR acquisitions of two full-polarimetric SAR images, observed with a spatial baseline, is time-consuming and on some occasions can procure unwanted statistical decorrelation. The results are appreciably improved with respect to classical polarimetric segmentation activities performed processing only one SAR product. The MCA analysis confirms the feasibility to resolve the volume-oriented indetermination problem and the results could have the same robustness as the method proposed in Laurent and Maxim (2008), which uses two PolInSAR products acquired using an ad-hoc dimensioned spatial geometry.

Disclosure statement

No potential conflict of interest was reported by the author.

References

- Alessandro, F., P. Claudio, and F. Rocca. 2001. "Permanent Scatterers in SAR Interferometry." *IEEE Transactions on Geoscience and Remote Sensing* 39 (1, January): 8–20. doi:[10.1109/36.898661](https://doi.org/10.1109/36.898661).
- Anthony, F., and L. Durden Stephen. 1998. "A Three-Component Scattering Model for Polarimetric SAR Data." *IEEE Transactions on Geoscience and Remote Sensing* 36 (3, May): 963–973. doi:[10.1109/36.673687](https://doi.org/10.1109/36.673687).
- Biondi, F. 2016. "Low Rank Plus Sparse Decomposition of Synthetic Aperture Radar Data for Maritime Surveillance." In *4th International Workshop on Compressed Sensing Theory and Its Applications to Radar, Sonar and Remote Sensing (Cosera)*, 75–79. IEEE. <https://ieeexplore.ieee.org/document/7745703>
- Chen, S., M. Ohki, M. Shimada, and M. Sato. 2013. "Deorientation Effect Investigation for Model-based Decomposition over Oriented Built-up Areas." In *IEEE Geoscience and Remote Sensing Letters* 10 (2): 273–277.
- Chen, S. W., and C. S. Tao. 2018. "PolSAR Image Classification Using Polarimetric-Feature-Driven Deep Convolutional Neural Network." *IEEE Geoscience and Remote Sensing Letters* 15 (4): 627–631. doi:[10.1109/LGRS.2018.2799877](https://doi.org/10.1109/LGRS.2018.2799877).
- Chen, S. W., X. S. Wang, S. P. Xiao, and M. Sato. 2014. "General Polarimetric Model-Based Decomposition for Coherency Matrix." *IEEE Transactions on Geoscience and Remote Sensing* 52 (3): 1843–1855. doi:[10.1109/TGRS.2013.2255615](https://doi.org/10.1109/TGRS.2013.2255615).
- Cloude Shane Robert. 2006. "Polarization Coherence Tomography." *Radio Science* 41 (4): RS4017.
- Cloude Shane Robert. 2007. "Dual-Baseline Coherence Tomography." *IEEE Geoscience and Remote Sensing Letters* 4 (1): 127–131. doi:[10.1109/LGRS.2006.885893](https://doi.org/10.1109/LGRS.2006.885893).
- David, B.-B. J., and M. Lopez-Sanchez Juan. 2010. "Applying the Freeman-Durden Decomposition Concept to Polarimetric SAR Interferometry." *IEEE Transactions on Geoscience and Remote Sensing* 48 (1, January): 466–479. doi:[10.1109/TGRS.2009.2024304](https://doi.org/10.1109/TGRS.2009.2024304).
- Elise, C., T.-S. Ccile, and W. Tabbara. 2006. "An Interferometric Coherence Optimization Method in Radar Polarimetry for High-Resolution Imagery." *IEEE Transactions on Geoscience and Remote Sensing* 44 (1, January): 167–175. doi:[10.1109/TGRS.2005.859357](https://doi.org/10.1109/TGRS.2005.859357).
- Fabio, B., G. V. Martino, R. Alberto, and V. Nicola. 2013. "Multi-Chromatic Analysis of InSAR Data." *IEEE Transactions on Geoscience and Remote Sensing* 51 (9): 4790–4799. doi:[10.1109/TGRS.2012.2230633](https://doi.org/10.1109/TGRS.2012.2230633).
- Ferro-Famil, L., H. Skriver, P. Lumsdon, R. Moshammer, and P. Kostas. 2005. "Forest Mapping and Classification Using L-Band PolInSAR Data." In *In POLinSAR Workshop*, 1–9. <http://adsabs.harvard.edu/full/2005ESASP.586....9F>
- Ferro-Famil, L., and N. Maxim. June 2–5, 2008. "Recent Advances in the Derivation of POL-InSAR Statistics: Study and Applications." *7th European Conference on Synthetic Aperture Radar*. Graf-Zeppelin-Haus, Friedrichshafen, Germany.

- Ferro-Famil, L., P. Eric, F. Kugler, and L. Jong-Sen. 2006. "Forest Mapping and Classification at L-Band Using Pol-InSAR Optimal Coherence Set Statistics." In *Proceedings of EUSAR 2006*, 16–18. Dresden: Germany. May. https://www.dlr.de/hr/en/desktopdefault.aspx/tabid-2330/3699_read-5521/
- Ferro-Famil, L., P. Eric, and L. Jong-Sen. July 2001b. "Unsupervised Classification and Analysis of Natural Scenes from Polarimetric Interferometric SAR Data." *Proceedings of the IEEE International Geoscience and Remote Sensing Symposium*. 6, 2715–2717. <https://ieeexplore.ieee.org/abstract/document/978139>
- Ferro-Famil, L., P. Eric, and L. Jong-Sen. 2001a. "Unsupervised Classification of Multifrequency and Fully Polarimetric SAR Images Based on H/A/Alpha-Wishart Classifier." *IEEE Transactions on Geoscience and Remote Sensing* 39 (11, Nov): 2332–2342. doi:[10.1109/36.964969](https://doi.org/10.1109/36.964969).
- Freeman, A. 2007. "Fitting a Two-Component Scattering Model to Polarimetric SAR Data from Forests." *IEEE Transactions on Geoscience and Remote Sensing* 45 (8, Aug): 2583–2592. doi:[10.1109/TGRS.2007.897929](https://doi.org/10.1109/TGRS.2007.897929).
- Gulab, S., Y. Yoshio, and P. Sang-Eun. 2013. "General Four-Component Scattering Power Decomposition with Unitary Transformation of Coherency Matrix." *IEEE Transactions on Geoscience and Remote Sensing* 51 (5, May): 3014–3022. doi:[10.1109/TGRS.2012.2212446](https://doi.org/10.1109/TGRS.2012.2212446).
- Jong-Sen, L., and L. Ainsworth Thomas. 2011. "The Effect of Orientation Angle Compensation on Coherency Matrix and Polarimetric Target Decompositions." *IEEE Transactions on Geoscience and Remote Sensing* 49 (1, January): 53–64. doi:[10.1109/TGRS.2010.2048333](https://doi.org/10.1109/TGRS.2010.2048333).
- Jong-Sen, L., L. Schuler Dale, L. Ainsworth Thomas, K. Ernst, K. Dayalan, and B. Wolfgang-Martin. 2002. "On the Estimation of Radar Polarization Orientation Shifts Induced by Terrain Slopes." *IEEE Transactions on Geoscience and Remote Sensing* 40 (1, January): 30–41. doi:[10.1109/36.981347](https://doi.org/10.1109/36.981347).
- Jong-Sen, L., R. Grunes Mitchell, L. Ainsworth Thomas, D. Li-Jen, L. Schuler Dale, and R. Cloude Shane. 1999a. "Unsupervised Classification Using Polarimetric Decomposition and the Complex Wishart Classifier." *IEEE Transactions on Geoscience and Remote Sensing* 37 (5): 2249–2258. doi:[10.1109/36.789621](https://doi.org/10.1109/36.789621).
- Jong-Sen, L., R. Grunes Mitchell, L. Ainsworth Thomas, L. Du, L. Schuler Dale, and C. S. Robert. 1999. "Unsupervised Classification of Polarimetric SAR Images by Applying Target Decomposition and Complex Wishart Distribution." *IEEE Transactions on Geoscience and Remote Sensing* 37 (5, September): 2249–2258. doi:[10.1109/36.789621](https://doi.org/10.1109/36.789621).
- Jong-Sen, L., R. Grunes Mitchell, P. Eric, and L. Ferro-Famil. 2004. "Unsupervised Terrain Classification Preserving Polarimetric Scattering Characteristics." *IEEE Transactions on Geoscience and Remote Sensing* 42 (4, April): 722–731. doi:[10.1109/TGRS.2003.819883](https://doi.org/10.1109/TGRS.2003.819883).
- Kostinski Alexander, B., and B. Wolfgang-Martin. 1986. "On Foundations of Radar Polarimetry." *IEEE Transactions on Geoscience and Remote Sensing* 34 (12): 1395–1404.
- Lee, J. S., M. R. Grunes, and E. Pottier. 2001. "Quantitative Comparison of Classification Capability: Fully Polarimetric versus Dual and Single-Polarization SAR." *IEEE Transactions on Geoscience and Remote Sensing* 39 (11): 2343–2351. doi:[10.1109/36.964970](https://doi.org/10.1109/36.964970).
- Lee, J.-S., D. L. Schuler, and T. L. Ainsworth. 2000. "Polarimetric SAR Data Compensation for Terrain Azimuth Slope Variation." *IEEE Transactions on Geoscience and Remote Sensing* 38 (5, September): 2153–2163. doi:[10.1109/36.868874](https://doi.org/10.1109/36.868874).
- Lopez-SanchezJuan, M., B.-B. J. David, and Y. Marquez-Moreno. 2007. "Model Limitations and Parameter-Estimation Methods for Agricultural Applications of Polarimetric SAR Interferometry." *IEEE Transactions on Geoscience and Remote Sensing* 45 (11, Nov): 3481–3493. doi:[10.1109/TGRS.2007.900690](https://doi.org/10.1109/TGRS.2007.900690).
- Madsen, S. N., and H. A. Zebker. 1992. *Automated Absolute Phase Retrieval in Across-Track Interferometry*. <https://ntrs.nasa.gov/search.jsp?R=19930063990>
- Maxim, N., F.-F. Laurent, and A. Reigber. 2008. "Multibaseline Polarimetric SAR Interferometry Coherence Optimization." *IEEE Geoscience and Remote Sensing Letters* 5 (1, January): 93–97. doi:[10.1109/LGRS.2007.908885](https://doi.org/10.1109/LGRS.2007.908885).
- Maxim, N., F.-F. Laurent, and A. Reigber. 2010. "Estimation of Forest Structure, Ground, and Canopy Layer Characteristics from Multibaseline Polarimetric Interferometric SAR Data." *IEEE*

- Transactions on Geoscience and Remote Sensing* 48 (4, March): 1086–1104. doi:[10.1109/TGRS.2009.2031101](https://doi.org/10.1109/TGRS.2009.2031101).
- Moreira, A. 1992. "Real-Time Synthetic Aperture Radar (SAR) Processing with a New Subaperture Approach." *IEEE Transactions on Geoscience and Remote Sensing* 30 (4): 714722. doi:[10.1109/36.158865](https://doi.org/10.1109/36.158865).
- Papathanassiou Konstantinos, P., and R. Cloude Shane. 2001. "Single-Baseline Polarimetric SAR Interferometry." *IEEE Transactions on Geoscience and Remote Sensing* 39 (11, Nov): 2352–2363. doi:[10.1109/36.964971](https://doi.org/10.1109/36.964971).
- Ridha, T. 2007. "Target Scattering Decomposition in Terms of Roll-Invariant Target Parameters." *IEEE Transactions on Geoscience Remote Sensing* 45 (1): 73–84. doi:[10.1109/TGRS.2006.886176](https://doi.org/10.1109/TGRS.2006.886176).
- Robert, C. S., and E. Pottier. 1996. "A Review of Target Decomposition Theorems in Radar Polarimetry." *IEEE Transactions on Geoscience and Remote Sensing* 34 (2, March): 498–518. doi:[10.1109/36.485127](https://doi.org/10.1109/36.485127).
- Robert, C. S., and E. Pottier. 1997. "An Entropy Based Classification Scheme for Land Applications of Polarimetric SARs." *IEEE Transactions on Geoscience Remote Sensing* 35 (1, January): 68–78. doi:[10.1109/36.551935](https://doi.org/10.1109/36.551935).
- Robert, C. S., and P. Papathanassiou Konstantinos. 1998. "Polarimetric SAR Interferometry." *IEEE Transactions on Geoscience and Remote Sensing* 36 (5, Sep): 1551–1565. doi:[10.1109/36.718859](https://doi.org/10.1109/36.718859).
- Sergi, D., B. Helko, B. Ulrich, and A. Parizzi. 2015. "Absolute Height Estimation Using a Single TerraSAR-X Staring Spotlight Acquisition." *IEEE Geoscience and Remote Sensing Letters* 12 (8, August): 1735–1739. doi:[10.1109/LGRS.2015.2422893](https://doi.org/10.1109/LGRS.2015.2422893).
- Si-Wei, C., W. Xue-Song, and S. Motoyuki. 2016. "Urban Damage Level Mapping Based on Scattering Mechanism Investigation Using Fully Polarimetric SAR Data for the 3.11 East Japan Earthquake." *IEEE Transactions on Geoscience Remote Sensing* 54 (12): 6919–6929. doi:[10.1109/TGRS.2016.2588325](https://doi.org/10.1109/TGRS.2016.2588325).
- Tao, C., S. Chen, Y. Li, and S. Xiao. 2017. "PolSAR Land Cover Classification Based on Roll-Invariant and Selected Hidden Polarimetric Features in the Rotation Domain." *Remote Sensing* 9 (7): 660. doi:[10.3390/rs9070660](https://doi.org/10.3390/rs9070660).
- Van Zyl, J. J. 1993. "Application of Cloude's Target Decomposition to Polarimetric Imaging Radar Data." In *Radar Polarimetry*. Vol. 1748, 184–192. International Society for Optics and Photonics. <https://www.spiedigitallibrary.org/conference-proceedings-of-spie/1748/0000/Application-of-Cloudes-target-decomposition-theorem-to-polarimetric-imaging-radar/10.1117/12.140615.short?SSO=1>
- Van Zyl Jakob, J., A. Motofumi, and Y. Kim. 2011. "Model-Based Decomposition of Polarimetric SAR Covariance Matrices Constrained for Nonnegative Eigenvalues." *IEEE Transactions on Geoscience and Remote Sensing* 49 (9, September): 3452–3459. doi:[10.1109/TGRS.2011.2128325](https://doi.org/10.1109/TGRS.2011.2128325).
- Wentao, A., Y. Cui, and J. Yang. 2010. "Three-Component Model-Based Decomposition for Polarimetric SAR Data ." *IEEE Transactions on Geoscience and Remote Sensing* 48 (6, June): 2732–2739. doi:[10.1109/TGRS.2010.2041242](https://doi.org/10.1109/TGRS.2010.2041242).
- Yoshio, Y., M. Toshifumi, I. Motoi, and H. Yamada. 2005. "Four-Component Scattering Model for Polarimetric SAR Image Decomposition." *IEEE Transactions on Geoscience and Remote Sensing* 43 (8, Aug): 1699–1706. doi:[10.1109/TGRS.2005.852084](https://doi.org/10.1109/TGRS.2005.852084).
- Yoshio, Y., M. Toshifumi, I. Motoi, and H. Yamada. 2006. "A Four-Component Decomposition of POLSAR Images Based on the Coherency Matrix." *IEEE Transactions on Geoscience and Remote Sensing* 3 (3, July): 292–296. doi:[10.1109/LGRS.2006.869986](https://doi.org/10.1109/LGRS.2006.869986).
- Yoshio, Y., S. Akinobu, B. Wolfgang-Martin, S. Ryoichi, and H. Yamada. 2011. "Four-Component Scattering Power Decomposition with Rotation of Coherency Matrix." *IEEE Transactions on Geoscience and Remote Sensing* 49 (6, June): 2251–2258. doi:[10.1109/TGRS.2010.2099124](https://doi.org/10.1109/TGRS.2010.2099124).
- Zhang, L., G. Wang, Z. Qiao, and H. Wang. 2017. "Azimuth Motion Compensation with Improved Subaperture Algorithm for Airborne SAR Imaging." *IEEE Journal of Selected Topics in Applied Earth Observations and Remote Sensing* 10 (1): 184–193. doi:[10.1109/JSTARS.2016.2577588](https://doi.org/10.1109/JSTARS.2016.2577588).